

# Self-aligning polar active matter

Paul Baconnier<sup>✉</sup>

*Gulliver UMR CNRS 7083, ESPCI Paris, PSL Research University,  
10 rue Vauquelin, 75005 Paris, France,  
AMOLF, Science Park 104, Amsterdam 1098XG, The Netherlands,  
and Lorentz Institute, Leiden University, Niels Bohrweg 2,  
CA Leiden 2333, The Netherlands*

Olivier Dauchot<sup>✉</sup>

*Gulliver UMR CNRS 7083, ESPCI Paris, PSL Research University,  
10 rue Vauquelin, 75005 Paris, France*

Vincent Démery<sup>✉</sup>

*Gulliver UMR CNRS 7083, ESPCI Paris, PSL Research University,  
10 rue Vauquelin, 75005 Paris, France and Laboratoire de Physique,  
Université de Lyon, École Normale Supérieure de Lyon,  
CNRS, Lyon 69342, France*

Gustavo Düring<sup>✉</sup>

*Instituto de Física, Pontificia Universidad Católica de Chile, 8331150 Santiago, Chile*

Silke Henkes<sup>✉</sup>

*Lorentz Institute, Leiden University, Niels Bohrweg 2, CA Leiden 2333, The Netherlands*

Cristián Huepe<sup>✉</sup>

*School of Systems Science, Beijing Normal University, Beijing, People's Republic of China,  
Northwestern Institute on Complex Systems and ESAM, Northwestern University,  
Evanston, Illinois 60208, USA,  
and CHuepe Labs, 2713 West Augusta Boulevard, Suite 1, Chicago, Illinois 60622, USA*

Amir Shee<sup>✉</sup>

*Northwestern Institute on Complex Systems and ESAM, Northwestern University,  
Evanston, Illinois 60208, USA*

 (published 20 March 2025)

Self-alignment describes the property of a polar active unit to align or antialign its orientation toward its velocity. In contrast to mutual alignment, where the headings of multiple active units tend to directly align with each other—as in the Vicsek model—self-alignment impacts the dynamics at the individual level by coupling the rotation and displacements of each active unit. This enriches the dynamics even in the absence of interactions and allows, for example, a single self-propelled particle to orbit in a harmonic potential. At the collective level, self-alignment modifies the nature of the transition to collective motion already in the mean-field description and can lead to other forms of self-organization such as collective actuation in dense or solid elastic assemblies of active units. This has significant implications for the study of dense biological systems, metamaterials, and swarm robotics. Here a number of models are reviewed that were introduced independently to describe the previously overlooked property of self-alignment and some of its experimental realizations are identified. The aim of this review is threefold: (i) to underline the importance of self-alignment in active systems, especially in the context of dense populations of active units and active solids; (ii) to provide a unified mathematical and conceptual framework for the description of self-aligning systems; and (iii) to discuss the common features and specific differences of the existing models of self-alignment. The review concludes by discussing promising research avenues in which the concept of self-alignment could play a significant role.

DOI: [10.1103/RevModPhys.97.015007](https://doi.org/10.1103/RevModPhys.97.015007)

## CONTENTS

I. Introduction	2
II. Self-Alignment: A Torque Coupling Orientation and Displacement	4
A. Symmetry considerations	4
B. Equations of motion	4
III. Individual Self-Aligning Agent Dynamics	6
A. Simple experiments with mechanical walkers	6
B. A self-aligning walker in a harmonic potential	7
C. Other realizations of self-alignment	7
1. Off-centered mechanical forces	7
2. Microswimmers	8
3. Migrating cells	8
IV. Collective Motion of Self-Aligning Agents	9
A. Liquids of self-aligning agents	9
B. Collective motion in a confining potential	11
C. Collective motion in active Voronoi models	12
D. Collective motion in a crystal of self-aligning disks	13
E. Collective motion of active elastic sheets	13
V. Collective Actuation of Active Elastic Materials	15
A. Selective and collective actuation in elastic lattices	15
B. Active jamming	16
C. Active Voronoi models in confinement	17
D. Mechanical oscillations in bacterial colonies and tissues	17
VI. Discussion and Perspectives	18
A. A unified framework?	18
B. Large-scale hydrodynamics theory	18
C. Connection with nonreciprocal phase transitions	19
D. Further perspectives	20
VII. Conclusion	21
Appendix A: Mechanisms for Self-Alignment	22
1. Self-alignment of axisymmetric rigid walkers	22
2. Self-alignment through nonaxisymmetric forces	22
Appendix B: Self-Aligning Active Particle in a Harmonic Potential with Isotropic Damping	23
1. General model	23
2. Stationary solutions	23
3. Stability analysis of the frozen state	23
4. Conclusion	24
Appendix C: Self-Aligning Active Particle in a Harmonic Potential with Anisotropic Damping	24
1. General model	24
2. Stationary solutions	24
3. Conclusion	24
References	24

## I. INTRODUCTION

Active matter is a class of nonequilibrium many-body systems that consist of individual energy-transducer components. The collective dynamics of such active entities underlies phenomena on scales ranging from the molecular to the macroscopic and includes both living and nonliving systems. Freed from the constraints of equilibrium dynamics, these systems exhibit a wealth of interesting large-scale behavior, such as motility-induced phase separation (Cates and Tailleur, 2015), collective motion (Vicsek and Zafeiris, 2012), active turbulence (Alert, Casademunt, and Joanny, 2022), collective actuation (Baconnier *et al.*, 2022), nonreciprocal phase separation (Fruchart *et al.*, 2021), and odd elasticity

(Scheibner *et al.*, 2020). The field of active matter focuses on understanding how the collective behaviors of such internally driven components can give rise to these large-scale patterns of motion or stress.

When the active units convert energy into a motion, or force, in the direction of a unit vector attached to and specific to each unit—its polarity—one talks about polar active matter. The microscopic degrees of freedom are then twofold: those describing the position of each active unit and those describing the orientation or the polarity of its self-propulsion force. The simplest case of polar active matter is the so-called scalar active matter (Wittkowski *et al.*, 2014): the interactions among the active units do not affect their orientation and are typically given by the usual attraction and/or repulsion forces. Scalar active matter is the simplest setting in which motility-induced phase separation (MIPS) can emerge (Cates and Tailleur, 2015). In more general cases, the presence of orientational degrees of freedom encoded in the polarity of the active units allows for additional types of interactions such as mutual alignment, which in turn can lead to the emergence of collective motion or collective actuation.

The field of active matter actually came into being with the introduction of the Vicsek model (Vicsek *et al.*, 1995) to study the emergence of large-scale collective dynamics in an out-of-equilibrium system inspired by bird flocks. As Vicsek *et al.* stated, “[T]he only rule of the model is that at each time step a given particle driven with a constant absolute velocity assumes the average direction of motion of the particles in its neighborhood with some random perturbation added.” It is important to realize that the Vicsek model does not specify the origin of the mutual alignment among its agents. As such, it must be seen as an effective model, the strength of which is to potentially encompass a large class of systems (Vicsek and Zafeiris, 2012) that includes schools of fish (Niwa, 1994), herds of quadrupeds (Ginelli *et al.*, 2015), flocks of flying birds (Cavagna and Giardina, 2014), bacterial colonies (Zhang *et al.*, 2010), actin filaments (Schaller *et al.*, 2010), vibrated polar disks (Deseigne, Dauchot, and Chaté, 2010), and rolling colloids (Bricard *et al.*, 2013).

Whether of physical or social origin, the mutual alignment of the velocity is most often seen as the consequence of pairwise interactions that directly couple the orientational degrees of freedom of the agents. For instance, self-propelled rods tend to align because steric repulsion forces induce an explicit pairwise torque on their bodies (Peruani, Deutsch, and Bär, 2006; Ginelli *et al.*, 2010; Peruani *et al.*, 2011), the conservation of momentum in inelastic collisions of spherical self-propelled particles imposes an alignment of the velocities (Grossman, Aranson, and Jacob, 2008), and birds are thought to align because they try to match their neighbors’ velocities due to “social forces.” General reviews on active systems with mutual alignment were given by Toner, Tu, and Ramaswamy (2005), Jülicher *et al.* (2007), Ramaswamy (2010), Marchetti *et al.* (2013), and Doostmohammadi *et al.* (2018).

However, this is not always the case: there are various models of self-propelled agents that produce collective motion and have interactions that depend on relative positions instead of relative angles since they require no explicitly aligning interaction. For example, collective motion can be driven by escape-pursuit dynamics (Romanczuk, Couzin, and

Schimansky-Geier, 2009) or by the deformation of self-propelled soft particles with local repulsion (Menzel and Ohta, 2012).

Finally, a different and mostly overlooked way to introduce interactions that involve the polarity of active units is to consider the possibility of couplings between orientations and translations. Our particular case of interest is self-alignment, where the orientation of each polar particle couples to its own translational degrees of freedom, more specifically to its velocity. Self-alignment was introduced as early as 1996 in a pioneering work (Shimoyama *et al.*, 1996) stemming from the basic observation that the polar self-driven headings and velocities of the active units do not have to be parallel. It was only ten years later that it was reintroduced by Szabó *et al.* (2006) to describe the collective migration of tissue cells.

The next decade saw the sporadic reintroduction of self-alignment in a variety of contexts. Henkes, Fily, and Marchetti (2011) used it to study active jamming, motivated by *in vitro* experiments on confluent monolayers of migratory epithelial and endothelial cells. It was part of a decentralized control algorithm for a wheeled robot swarm formation implemented by Ferrante *et al.* (2012) that led to a minimal model of active elastic solids composed of self-driven agents linked by permanent springs (Ferrante *et al.*, 2013a). It was found to result from the mechanical vibration of mechanically polar disks and shown to be the key ingredient for the emergence of collective motion in this system (Deseigne, Dauchot, and Chaté, 2010; Weber *et al.*, 2013).

Indeed, it was long assumed that self-alignment was a curiosity of the single-particle dynamics that could be treated as effective mutual alignment at the collective level. The flocking dynamics of systems with self-alignment has been investigated in some detail. It is not robust to dissenters (Yllanes, Leoni, and Marchetti, 2017) and it interacts with motility-induced phase separation (Sese-Sansa, Pagonabarraga, and Levis, 2018) and glass formation, as it is able to produce flocking glass phases (Paoluzzi, Levis, and Pagonabarraga, 2024). It has also continued as a model for flocking in confluent epithelial cell sheets with the use of particle models (Giavazzi *et al.*, 2017) and Voronoi vertex models (Malinverno *et al.*, 2017; Giavazzi *et al.*, 2018). It has also been proposed for the complex migration of the simple animal *Trichoplax* (Bull, Prakash, and Prakash, 2021; Davidescu *et al.*, 2023). Only recently has self-alignment started to attract more attention in the context of dense and solid active matter, where it often leads to collective dynamics that are distinct from those observed for polar mutual alignment. It has now been shown that novel collective effects can emerge if the structure of the assembly remains frozen on long timescales due to confinement or cohesion, when the system behaves like an elastic solid rather than a viscous liquid.

In the most general sense, active solids are materials that exhibit dynamic behavior due to internal out-of-equilibrium processes, which causes them to undergo not only changes in shape, size, and other physical properties but also dynamical transitions. Here are a few examples where self-alignment has proven to be a key ingredient for the observed dynamics. In the context of epithelial cell sheets, self-alignment induces collective oscillations in Voronoi vertex models (Barton *et al.*, 2017; Petrolli *et al.*, 2019) and phase-field models (Peyret

*et al.*, 2019). In dense biofilms where the active units can be modeled as embedded in an elastic network, it also leads to various forms of collective oscillations (Xu *et al.*, 2023). In artificially designed active elastic metamaterials, where self-driven components are coupled through a network of mechanical links, self-alignment leads to different forms of collective motion and collective actuation (in which agents perform large-scale oscillations around a reference configuration) that strongly depend on the network properties (Ferrante *et al.*, 2013b; Woodhouse, Ronellenfitsch, and Dunkel, 2018; Turgut *et al.*, 2020; Baconnier *et al.*, 2022; Zheng *et al.*, 2023). More recently, a complex interplay between self-alignment and the active glass transition was reported (Paoluzzi, Levis, and Pagonabarraga, 2024). Finally, self-alignment has increasing applications for decentralized control in the context of swarm robotics owing to its emergent collective dynamics and the potential simplicity of its implementation (Zheng, Huepe, and Han, 2020; Ben Zion *et al.*, 2023). Broadly speaking, the coupling between the individual orientational degrees of freedom and the translational ones, as provided by self-alignment, opens the path toward the design of spontaneous oscillating dynamics in strongly damped systems. As such, self-alignment is a good candidate for explaining oscillating dynamics in various living systems; it opens the path toward the design of new smart materials (Spillman, Sirkis, and Gardiner, 1996; Bahl *et al.*, 2020) and offers a new paradigm when one develops algorithms for swarms robotics, taking advantage of simple morphological rules (Pfeifer, 2006; Garattoni and Birattari, 2016).

The purpose of this review is to provide a unifying overview on the various phenomena, underlying mechanisms, emergent features, and applications related to self-alignment in different fields of active matter. More specifically, our first goal is to underline the importance of self-alignment, especially in the context of dense and solid active units. We describe the mechanical origin of self-alignment and discuss current experiments that demonstrate the role of self-alignment in emerging collective phenomena. Our second goal is to provide a common mathematical framework for the description of self-aligning systems. Finally, reviewing the existing models that include self-alignment, we aim at discussing their similarities and differences in the context of this common framework.

The review is organized as follows. In Sec. II we define the concept of self-alignment and explain its mechanical origin. We introduce the general forms of the equations of motion for self-aligning polar active agents and how they simplify in several contexts. Section III describes the experimental and theoretical works that have analyzed the self-aligning dynamics of single agents and discusses different ways in which self-alignment can be implemented. In Sec. IV we review different situations where self-alignment leads to collective motion in active liquids in the absence of other sources of mutual alignment between the agents. Section V describes various experimental and numerical contexts in which collective actuation has been observed in dense or solid active systems with self-aligning dynamics. Finally, in Sec. VI we discuss unifying perspectives that connect the different types of self-aligning dynamics presented in this review with each other

and with other novel forms of active dynamics that have been introduced in the literature.

## II. SELF-ALIGNMENT: A TORQUE COUPLING ORIENTATION AND DISPLACEMENT

### A. Symmetry considerations

A precise mechanical argument for the origin of self-alignment is provided later in the review using a mechanical walker model. We first provide an intuition of it while following simple symmetry considerations. Suppose that one aims at designing the most rudimentary possible self-propelled polar agent. While the shape of its body could remain isotropic (circular in two dimensions and spherical in three dimensions), one would need to embed a unit vector  $\hat{n}$  describing the tailhead axis of the agent, also called the polar axis, along which it gains momentum due to self-propulsion; see Fig. 1. To ensure an unbiased motion of a polar active agent, its design, namely, the distribution of mass, but also the spatial distribution of propulsive and dissipative forces must respect the axial symmetry of the body so that no systematic torque is exerted on the agent when it moves along its polar axis. It is then clear that the same distribution of propulsive and dissipative forces are not axially symmetric with respect to the direction of motion, as soon as the latter is not aligned with the polar axis. This asymmetric distribution of forces generically exerts a torque on the agent body, which thus rotates its polar axis toward the direction of motion or its opposite; this is self-alignment.

For instance, the vibrated polar disks introduced by Deseigne, Dauchot, and Chaté (2010) have two contacts with the vibrating ground: a large piece of rubber and a thin metallic tip. The rubber piece is responsible for most of the friction. As soon as the disk moves in a direction that is not aligned with its polar axis, the asymmetric friction on the ground makes it rotate toward its direction of motion. In the case of Hexbugs [see the top image in Fig. 2(b)] or bristlebots (Giomi, Hawley-Weld, and Mahadevan, 2013), legs are bent toward the front. While it is more difficult to separate the dissipative from the propulsive elements, the aforementioned generic symmetry argument still holds.

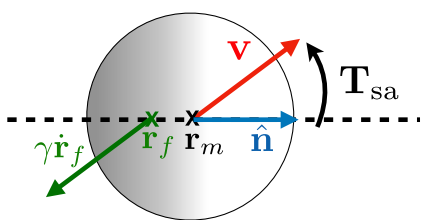


FIG. 1. Schematic representation of self-alignment. A particle with a polar distribution of friction  $\gamma(\mathbf{r})$ , as indicated by the gray shaded area, has an axial symmetry (the dotted line) along the direction of its polar vector  $\hat{n}$ . For clarity, the distribution of mass is supposed to be homogeneous, and the distribution of active forces leading to the active force  $F_a \hat{n}$  acting at the center of mass  $\mathbf{r}_m$  is not represented. When the velocity  $\mathbf{v} = \dot{\mathbf{r}}$  is not aligned with  $\hat{n}$ , the friction force  $\gamma \dot{\mathbf{r}}_f$  acting on the center of friction  $\mathbf{r}_f$  is not aligned with  $\hat{n}$ , leading to a self-aligning torque  $\mathbf{T}_{sa}$ .

As we later see, the sign of the self-aligning torque depends on the distribution of the friction forces relative to the distribution of mass: when the agent experiences more friction on the back than on the front, it spontaneously aligns toward its velocity, while it antialigns in the opposite case. It is therefore possible to set the sign of the self-alignment by design (Ben Zion *et al.*, 2023).

### B. Equations of motion

We now make the aforementioned argument more precise, leaving a detailed calculation to Appendix A for clarity. We consider an arbitrary body of volume  $\mathcal{W}$ , held rigid by a distribution of pairwise internal forces  $f_{int}(\mathbf{r})$  with a distribution of mass  $\tilde{m}(\mathbf{r})$ , a distribution of friction coefficient  $\tilde{\gamma}(\mathbf{r})$ , and a distribution of active and external forces  $f_{act}(\mathbf{r})$  and  $f_{ext}(\mathbf{r})$  acting upon it. When we introduce the center of mass  $\mathbf{r}_m = (1/m) \int_{\mathcal{W}} \tilde{m}(\mathbf{r}) \mathbf{r} d\mathbf{r}$ , with  $m = \int_{\mathcal{W}} \tilde{m}(\mathbf{r}) d\mathbf{r}$ , the total mass, the center of friction  $\mathbf{r}_f = (1/\gamma) \int_{\mathcal{W}} \tilde{\gamma}(\mathbf{r}) \mathbf{r} d\mathbf{r}$ , with  $\gamma = \int_{\mathcal{W}} \tilde{\gamma}(\mathbf{r}) d\mathbf{r}$ , the effective friction coefficient, and  $J = \int_{\mathcal{W}} \tilde{m}(\mathbf{r}) |\mathbf{r} - \mathbf{r}_m|^2 d\mathbf{r}$  the angular moment of inertia, the equations of motion for this rigid body read

$$m \ddot{\mathbf{r}}_m = \mathbf{F}_a - \gamma \dot{\mathbf{r}}_f + \mathbf{F}_{ext}, \quad (1a)$$

$$J \dot{\Omega} = \mathbf{T}_a + \gamma (\mathbf{r}_m - \mathbf{r}_f) \times \dot{\mathbf{r}}_m - \gamma_r \Omega + \mathbf{T}_{ext}, \quad (1b)$$

with  $\dot{\mathbf{r}}_f = \dot{\mathbf{r}}_m + \Omega \times (\mathbf{r}_f - \mathbf{r}_m)$  and where  $\mathbf{F}_a = \int_{\mathcal{W}} f_{act}(\mathbf{r}) d\mathbf{r}$ ,  $\mathbf{F}_{ext} = \int_{\mathcal{W}} f_{ext}(\mathbf{r}) d\mathbf{r}$ ,  $\mathbf{T}_a = \int_{\mathcal{W}} (\mathbf{r} - \mathbf{r}_m) \times f_{act} d\mathbf{r}$ ,  $\mathbf{T}_{ext} = \int_{\mathcal{W}} (\mathbf{r} - \mathbf{r}_m) \times f_{ext} d\mathbf{r}$ ,  $\Omega$  is the solid body rotation vector, and  $\gamma_r = \int_{\mathcal{W}} \tilde{\gamma}(\mathbf{r}) |\mathbf{r} - \mathbf{r}_m|^2 d\mathbf{r}$  is the effective rotational damping coefficient. Note that the damping coefficients are usually taken as scalar but can also be tensorial for nonsymmetric shapes.

For a polar active particle whose active forces and friction distributions are symmetric with respect to the direction of the active force  $\hat{n}$ ,  $\mathbf{T}_a = \mathbf{0}$  and  $\mathbf{r}_m - \mathbf{r}_f \propto \hat{n}$ , so  $\gamma(\mathbf{r}_m - \mathbf{r}_f) = \zeta \hat{n}$ , leading to the general equations of motion for an achiral polar active particle,

$$m \ddot{\mathbf{r}}_m = F_a \hat{n} - \gamma \dot{\mathbf{r}}_f + \mathbf{F}_{ext}, \quad (2a)$$

$$J \dot{\Omega} = \zeta \hat{n} \times \dot{\mathbf{r}}_m - \gamma_r \Omega + \mathbf{T}_{ext}. \quad (2b)$$

Equation (2a) describes the inertial translational motion of an agent that is self-propelled by an active force  $F_a \hat{n}$  and is subjected to an external force  $\mathbf{F}_{ext}(\mathbf{r})$ . Equation (2b) demonstrates the presence of self-alignment in the form of a torque  $\mathbf{T}_{sa} = \zeta \hat{n} \times \dot{\mathbf{r}}_m$  that couples the orientation  $\hat{n}$  of the self-propulsive force to the velocity  $\dot{\mathbf{r}}$  of the agent. We again stress that this self-alignment is distinct from a mutual Vicsek alignment and is generically present for self-propelled polar particles.

Finally, these deterministic equations can be completed with noise. These noise terms need not satisfy Einstein's relation, since the agent is intrinsically out of equilibrium and the noise can thus take its source from the driving or from the dissipative interactions, in addition to the usual thermal bath,

when significant. The translational noise does not need to be isotropic either.

Historically, the equations of motion for self-aligning polar agents have been introduced on a phenomenological basis in several forms, with a variety of simplifications and approximations. First, all existing studies take place in two dimensions, where  $\hat{\mathbf{n}} = (\cos \theta, \sin \theta, 0)$  and  $\boldsymbol{\Omega} = \dot{\theta}\hat{z}$ , with  $\hat{z}$  the out-of-plane direction and  $\dot{\hat{\mathbf{n}}} = \boldsymbol{\Omega} \times \hat{\mathbf{n}}$ . Second, other than the work of Fersula, Bredeche, and Dauchot (2024), who reported unexpected effects of the coupling between angular inertia and self-alignment, the angular dynamics is assumed to be overdamped ( $J/\gamma_r \rightarrow 0$ ) because, for all active agents considered so far, the rotational damping is large because of the agent shape. In practice, the translational dynamics can also be taken in the overdamped limit, but this is not always the case, as the relaxation dynamics of the velocity can be of interest too.

Beyond these standard simplifications, all existing work has assumed the equality of the velocities of the center of mass and the center of friction  $\dot{\mathbf{r}}_f = \dot{\mathbf{r}}_m$ . Although this is not strictly valid in the presence of self-alignment, it is a reasonable assumption in the overdamped limit; see Appendix A. More importantly, the self-aligning torque was sometimes chosen to be proportional to the magnitude of the velocity or to solely depend on its orientation. In the following we need to distinguish these two formulations, which we do by writing

$$\mathbf{T}_{\text{sa}} = \zeta \hat{\mathbf{n}} \times \mathbf{w}, \quad (3)$$

with either  $\mathbf{w} = \mathbf{v} = \dot{\mathbf{r}}$  or  $\mathbf{w} = \hat{\mathbf{v}} = \dot{\mathbf{r}}/|\dot{\mathbf{r}}|$ . Altogether, our starting point equations of motion, for the purpose of this review, are

$$m\ddot{\mathbf{r}} = \mathbf{F}_a \hat{\mathbf{n}} - \gamma \dot{\mathbf{r}} + \mathbf{F}_{\text{ext}}(\mathbf{r}), \quad (4a)$$

$$\dot{\hat{\mathbf{n}}} = \beta(\hat{\mathbf{n}} \times \mathbf{w}) \times \hat{\mathbf{n}} + \frac{1}{\gamma_r} \mathbf{T}_{\text{ext}} \times \hat{\mathbf{n}}, \quad (4b)$$

along with their fully overdamped counterpart,

$$\dot{\mathbf{r}} = v_0 \hat{\mathbf{n}} + \frac{1}{\gamma} \mathbf{F}_{\text{ext}}(\mathbf{r}), \quad (5a)$$

$$\dot{\hat{\mathbf{n}}} = \beta(\hat{\mathbf{n}} \times \mathbf{w}) \times \hat{\mathbf{n}} + \frac{1}{\gamma_r} \mathbf{T}_{\text{ext}} \times \hat{\mathbf{n}}, \quad (5b)$$

with  $v_0 = F_a/\gamma$ . In the case with  $\mathbf{w} = \mathbf{v}$ , where the coupling is proportional to the magnitude of the velocity,  $\beta = \zeta/\gamma_r$  has the dimension of an inverse length scale  $l_a^{-1}$ , which we call the alignment length. In the case of  $\mathbf{w} = \hat{\mathbf{v}}$ , where the coupling is independent of the magnitude of the velocity,  $\beta$  has the dimension of an inverse timescale  $\tau_a^{-1}$ , which we call the

TABLE I. Self-alignment interactions as defined in the literature. The papers are grouped in two sets according to the choice of  $\mathbf{w} = \hat{\mathbf{v}}$  or  $\mathbf{w} = \mathbf{v}$  and are sorted chronologically in each set. The third, fourth, and fifth columns indicate whether the self-aligning coupling is linear (L) or nonlinear (NL), whether the damping is isotropic (Y) or anisotropic (N), and whether the system is studied under confinement (Y) or not (N). The sixth column specifies the type of “agent” or “system” considered, while the seventh column indicates the observed macroscopic phase flocking (F) or actuation (A).

Reference	$\mathbf{w}$	L/NL	Isotropic damping	Confinement	Type of system	Type of phase: Flocking (F) and/or actuation (A)
Shimoyama <i>et al.</i> (1996)	$\hat{\mathbf{v}}$	NL	Y	N	Particles	F
Szabó <i>et al.</i> (2006)	$\hat{\mathbf{v}}$	L	Y	N	Particles	F
Henkes, Fily, and Marchetti (2011)	$\hat{\mathbf{v}}$	L	Y	Y	Particles	F and A
Weber <i>et al.</i> (2013)	$\mathbf{v}$	NL	Y	N	Particles	F
Ferrante <i>et al.</i> (2013a)	$\mathbf{v}$	NL	N	N	Robots or structures	F
Camley and Rappel (2014)	$\hat{\mathbf{v}}$	L	Y	Y or N	Particles	F
Lam, Schindler, and Dauchot (2015b)	$\mathbf{v}$	NL	Y	N	Particles	F
Barton <i>et al.</i> (2017)	$\hat{\mathbf{v}}$	NL	Y	Y	Voronoi	F and A
Giavazzi <i>et al.</i> (2017)	$\hat{\mathbf{v}}$	L	Y	N	Cells or particles	F
Malinverno <i>et al.</i> (2017)	$\hat{\mathbf{v}}$	L	Y	N	Cells or Voronoi	F
Yllanes, Leoni, and Marchetti (2017)	$\hat{\mathbf{v}}$	L	Y	N	Particles	F
Giavazzi <i>et al.</i> (2018)	$\hat{\mathbf{v}}$	NL	Y	N	Voronoi	F
Sese-Sansa, Pagonabarraga, and Levis (2018)	$\hat{\mathbf{v}}$	NL	Y	N	Particles	F
Petrolli <i>et al.</i> (2019)	$\hat{\mathbf{v}}$	NL	Y	Y	Cells or Voronoi	A
Dauchot and Démery (2019)	$\mathbf{v}$	NL	Y	Y	Single particles	A
Peyret <i>et al.</i> (2019)	$\mathbf{v}$	L	Y	Y	Cells or phase fields	A
Lin, Han, and Huepe (2021)	$\mathbf{v}$	NL	N	N	Robots or structures	A
Bull, Prakash, and Prakash (2021)	$\mathbf{v}$	NL	Y	N	Cells or structures	F
Teixeira, Fernandes, and Brunnet (2021)	$\hat{\mathbf{v}}$	L	Y	N	Structures	F
Baconnier <i>et al.</i> (2022)	$\mathbf{v}$	NL	Y	Y	Structures	A
Damascena, Cabral, and de Souza Silva (2022)	$\mathbf{v}$	NL	Y	Y	Single particles	A
Davidescu <i>et al.</i> (2023)	$\hat{\mathbf{v}}$	NL	Y	N	Cells or Voronoi	F
Xu <i>et al.</i> (2023)	$\mathbf{v}$	NL	N	Y	Bacteria	A
Ben Zion <i>et al.</i> (2023)	$\mathbf{v}$	NL	N	Y	Robots	
Paoluzzi, Levis, and Pagonabarraga (2024)	$\mathbf{v}$	NL	Y	N	Particles	A
Baconnier, Démery, and Dauchot (2024)	$\mathbf{v}$	NL	Y	Y	Structures	A
Hernández-López <i>et al.</i> (2024)	$\mathbf{v}$	NL	Y	Y	Structures	F
Lazzari, Dauchot, and Brito (2024)	$\mathbf{v}$	NL	Y	Y	Structures	A

alignment time. Finally, a last variant of the angular dynamics consists in replacing it with a simple linear relaxation toward the velocity orientation  $\psi$ , as done by Szabó *et al.* (2006) and Henkes, Fily, and Marchetti (2011):  $\dot{\theta} = \beta(\psi - \theta)$ .

We conclude this section by making the connection between the previously introduced achiral self-aligning polar particles and the most familiar active Brownian particles, whose dynamics obey the following equations:

$$\dot{\mathbf{r}} = v_0 \hat{\mathbf{n}} + \frac{1}{\gamma} \mathbf{F}_{\text{ext}}(\mathbf{r}), \quad (6a)$$

$$\dot{\hat{\mathbf{n}}} = \frac{1}{\gamma_r} \mathbf{T}_{\text{ext}}(\mathbf{r}) + \sqrt{2D_r} \eta \hat{\mathbf{n}}^\perp, \quad (6b)$$

with the translational noise often neglected and the angular noise distribution Gaussian and  $\delta$  correlated. One readily sees that the active Brownian dynamics corresponds to the fully overdamped dynamics in the absence of self-alignment ( $\beta = 0$ ).

Table I provides a synthetic view of the main articles where self-alignment was introduced in the literature, which categorizes the variations in the equations of motion considered in each case. We group them according to whether  $\mathbf{w} = \mathbf{v}$  or  $\hat{\mathbf{v}}$ , whether the angular dynamics is linear, and whether the translational damping is isotropic.

### III. INDIVIDUAL SELF-ALIGNING AGENT DYNAMICS

#### A. Simple experiments with mechanical walkers

Vibrated or vibrating mechanical walkers, which are often used in the experimental study of polar active matter (Deseigne, Dauchot, and Chaté, 2010; Deseigne *et al.*, 2012; Giomi, Hawley-Weld, and Mahadevan, 2013; Baconnier *et al.*, 2022; Ben Zion *et al.*, 2023), generically exhibit self-alignment. This can be demonstrated in a simple experiment that imposes the translational velocity of the walker while leaving its polarity free to reorient. If the walker exhibits self-alignment, it will reorient along the imposed direction of motion. Such an experiment was conducted by Baconnier *et al.* (2022) in order to extract the parameters of the dynamics of individual Hexbugs; see Fig. 2(a). Using a simple mechanical device to drive the Hexbug along a square trajectory while allowing it to rotate freely, Baconnier *et al.* demonstrated for this system that  $\mathbf{w} = \dot{\mathbf{r}}$  and that self-alignment is controlled by an alignment length. Indeed, the angle between the polarity vector and the velocity vector decreases exponentially to zero after each change of imposed translational direction with a characteristic time  $\tau_a(V) \sim 1/V$ , where  $V$  is the imposed translational speed. This results in the measurement of an alignment length  $l_a = V\tau_a(V)$  that in this case is found to be of the order of one Hexbug body length.

An alternative manifestation of self-alignment can be observed when a constant external force is applied to the polar walker. In that case the velocity relaxes toward the sum

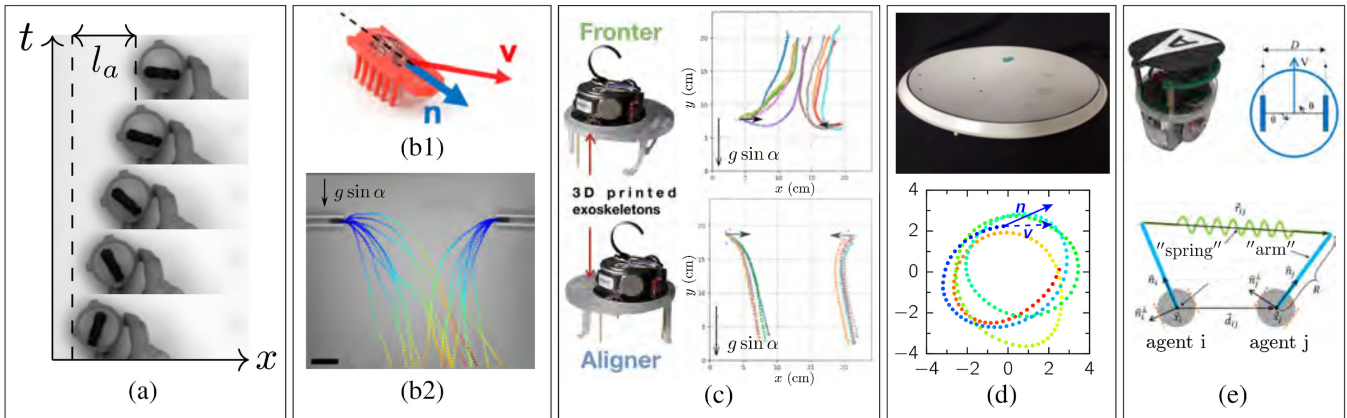


FIG. 2. Self-alignment in dynamics of single walkers. (a) When a self-aligning agent, here a Hexbug [see the top image in (b)], is manually translated in a different direction from that of its tailhead polarity, while remaining free to reorient, its orientation relaxes toward the direction of the imposed motion on a characteristic distance  $l_a$ . Adapted from Baconnier *et al.*, 2022. (b) Top image: a Hexbug with a velocity  $\hat{\mathbf{v}}$  that is not necessarily aligned with its tailhead polarity  $\hat{\mathbf{n}}$ . Bottom image: when moving on a plane inclined at an angle  $\alpha$  with respect to the horizontal, a Hexbug aligns in the direction of the gravity force; trajectories are color coded from blue to red as time increases. Adapted from Baconnier, 2023. (c) A kilobot (Rubenstein, Cornejo, and Nagpal, 2014) embedded in two morphologically distinct 3D-printed exoskeleton align either toward (bottom image) or against (top image) the direction of the gravity force, denoting a positive and a negative value of  $\beta$ , respectively; colors indicate different realizations of the trajectories. Adapted from Ben Zion *et al.*, 2023 with additional data. (d) Orbiting dynamics of a Hexbug in a parabolic dish; the trajectory is color coded from red to blue as time increases. Adapted from Dauchot and Démery, 2019. (e) Bottom image: schematic representation of the active elastic model for two interacting self-propelled agents. Each agent is represented by a gray disk with a blue “arm” projecting forward a distance  $R$ . The sinusoidal green line represents a linear spring connecting the tips of these arms. The agent positions and centers of rotations are given by  $x_i$  and  $x_j$ , while their heading polarities are indicated by the unit vectors  $\hat{\mathbf{n}}_i$  and  $\hat{\mathbf{n}}_j$ , respectively. . The dotted orange lines show the position of the wheels in a potential mechanical realization with actual robots, such as the one shown in the top images. Top images: From Zheng, Huepe, and Han, 2020. Bottom image: Adapted from Lin, Han, and Huepe, 2021.

of the active force and the external one. Since the polarity tends to align with the velocity, it will converge toward aligning with the external force. Experimentally, the simplest implementation of an external force consists in placing the active agent on a plane inclined by a small angle  $\alpha$  with respect to the horizontal, thereby imposing a constant force  $g \sin \alpha$  downhill. A Hexbug placed on such a tilted plane will therefore reorient its body downward along the slope; see Fig. 2(b). Note that the sign of the self-aligning torque is determined by the design of the walker's morphology. It can be positive, as is the case for Hexbugs, or negative, as recently illustrated by Ben Zion *et al.* (2023) and Casiulis *et al.* (2024) for the case of augmented Kilobots; see Fig. 2(c).

## B. A self-aligning walker in a harmonic potential

The importance of self-alignment is best illustrated by considering the dynamics of a self-aligning active particle in a harmonic potential. This canonical problem was studied by Dauchot and Démery (2019), who explored the dynamics of a Hexbug in a parabolic dish antenna; see Fig. 2(d). The deterministic dynamics of this system is described by Eq. (4) in the  $w = v$  case with external force  $F_{\text{ext}} = -kr$ , where  $k$  is the stiffness of the potential and  $r$  is the particle position with respect to its minimum. Note that here, as in Eq. (A4), the translational damping is assumed to be isotropic since the effect of the external forces on the velocity is independent of the particle orientation. A more detailed derivation of the dynamics in both the isotropic and anisotropic cases is included in Appendixes B and C, respectively.

We can rescale the dynamical equations by a characteristic length scale  $l_e = F_a/k$ , the “elastic length” at which the harmonic potential force is balanced by the active force, and by a characteristic timescale  $t_0 = \gamma/k$ . The resulting dimensionless equations of motion in the noiseless case then become

$$\tau_v \ddot{\mathbf{r}} = \hat{\mathbf{n}} - \dot{\mathbf{r}} - \mathbf{r}, \quad (7a)$$

$$\tau_n \dot{\hat{\mathbf{n}}} = (\hat{\mathbf{n}} \times \dot{\mathbf{r}}) \times \hat{\mathbf{n}}, \quad (7b)$$

with  $\tau_v = mk/\gamma^2$  and  $\tau_n = k/(\beta F_a) = l_a/l_e$ . In the overdamped case ( $\tau_v = 0$ ), Eqs. (7a) and (7b) admit an infinite set of fixed points ( $\dot{\mathbf{r}} = 0$  and  $\dot{\mathbf{n}} = 0$ ), where the agent sits at a distance  $r = 1$  from the origin, pointing radially, with  $\mathbf{r} = \hat{\mathbf{n}}$ . In the presence of noise, the agent diffuses along this continuous set of fixed points. These states, referred to as climbing states by Dauchot and Démery (2019), are marginally stable for  $\tau_n \geq 1$  and unstable for  $\tau_n < 1$ . For  $\tau_n < 1$  the fixed points leave place to a stable “orbiting” state, in which the active agent rotates in the trap along a circular orbit of radius  $r = \sqrt{\tau_n}$  with tangential velocity  $v_\theta = r\omega = \sqrt{1 - \tau_n}$ , where  $\omega$  is the angular velocity; see Fig. 2(d). The rotation is clockwise or counterclockwise, spontaneously breaking the chiral symmetry of the equation of motions. At the transition from the climbing state to the orbiting state, the amplitude of the oscillations is finite and the frequency is zero. This corresponds to a drift-pitchfork bifurcation (Kness, Tuckerman, and Barkley, 1992). Inertia does not affect the stability of the climbing state, which remains marginally

stable for  $\tau_n \geq 1$ . Inertia also does not affect the nature of the transition as long as  $\tau_v \leq 1$ . If we increase inertia beyond this threshold, the stable orbiting state appears at  $\tau_n$  values below  $\tau_n^* = \tau_v/[2\sqrt{\tau_v} - 1] \geq 1$ . Hence, the climbing and orbiting states coexist for  $1 \leq \tau_n \leq \tau_n^*$  and the transition becomes discontinuous.

In the overdamped limit, the aforementioned picture has been extended to the case of an anisotropic harmonic trap (Damascena, Cabral, and de Souza Silva, 2022). In this case the fixed points still form a loop, topologically speaking, but not a unit circle. They do not become unstable at the same level of activity: the fixed points in the stiffest parts of the trap destabilize first, and those in the shallowest parts destabilize last. The dynamical regimes are also more complex: instead of circles, the particle follows an oval for a weakly asymmetric potential, which deforms to a lemniscate and then to higher-order lemniscates upon increasing the asymmetry. There are two interesting limiting cases. When the soft direction becomes flat, the active unit polarizes in this direction and starts unbounded motion. When the hard direction becomes infinitely rigid, the orbiting state does not exist. It was also shown that, in the last case, the angular noise can still restore pseudoperiodic dynamics (Baconnier, Démery, and Dauchot, 2024).

Finally, we note that the case of antialigning active particles in a harmonic potential was reported by Ben Zion *et al.* (2023). In this case the climbing state becomes unconditionally stable and no orbiting solution emerges, leading to clustering on large scales (Casiulis *et al.*, 2024).

## C. Other realizations of self-alignment

### 1. Off-centered mechanical forces

A specific type of mechanical interaction that can lead to dynamics equivalent to self-alignment was considered by Lin, Han, and Huepe (2021). In this case, each active agent is subject to off-centered forces applied on a point  $\mathbf{r} + R\hat{\mathbf{n}}$  at the end of a lever arm of length  $R$  that projects forward from the center of rotation  $\mathbf{r}$ ; see Fig. 2(e). These forces will introduce a mechanical torque equal to

$$\mathbf{T}_{\text{ext}} = R\hat{\mathbf{n}} \times \mathbf{F}_{\text{ext}}(\mathbf{r} + R\hat{\mathbf{n}}). \quad (8)$$

The corresponding Newton's equations for these agents are thus equivalent to those in Eq. (2), but by replacing the self-aligning torque  $\mathbf{T}_{\text{sa}}$  with  $\mathbf{T}_{\text{ext}}$ . Note, however, that now the forces are not computed only as a function of particle positions; they will also depend on their orientations since the argument of  $\mathbf{F}_{\text{ext}}$  includes  $\hat{\mathbf{n}}$ . This is because the interaction forces now depend on the distance from lever arm to lever arm, rather than from center of rotation to center of rotation.

Lin, Han, and Huepe (2021) and Lin *et al.* (2023) showed that this dependency of  $\mathbf{F}_{\text{ext}}$  on  $R\hat{\mathbf{n}}$  results in several effects that are not found in self-aligning dynamics. For example, it allows the interaction to be set as based mainly on mutual alignment, for large  $R$ , or on self-alignment, for small  $R$ . It also results in states of quenched disorder that cannot form in self-aligning systems.

In a case with overdamped dynamics and isotropic translational damping, Eq. (6) becomes  $\dot{\mathbf{r}} = v_0 \hat{\mathbf{n}} + (1/\gamma) \mathbf{F}_{\text{ext}}(\mathbf{r} + R\hat{\mathbf{n}})$ . This can be inserted into Eq. (8) to obtain an expression for the torque akin to the self-alignment torque  $\mathbf{T}_{\text{sa}}$  in Eq. (3) for the  $\mathbf{w} = \dot{\mathbf{r}}$  case if we define  $\zeta = \gamma R$ . In the limit of small  $R$ , the resulting dynamics will then become identical to self-alignment. However, if the translational damping is anisotropic, this equivalence breaks down since the expression corresponding to Eq. (6) will be  $\gamma \dot{\mathbf{r}} = F_a \hat{\mathbf{n}} + \mathbf{F}_{\text{ext}}(\mathbf{r} + R\hat{\mathbf{n}})$ , where  $\gamma$  remains a tensor. In the limiting case with infinite translational damping along  $\hat{\mathbf{n}}^\perp$ , where no lateral displacements are allowed (as in the models of wheeled agents reviewed in Sec. IV.E), this difference is crucial because  $\hat{\mathbf{n}} \times \mathbf{w} = 0$  and the self-alignment torque in Eq. (5b) would vanish. By contrast, even in this limit, models based on off-centered forces will produce angular dynamics that resemble self-alignment since  $\mathbf{T}_{\text{ext}}$  will not vanish.

## 2. Microswimmers

Another potential realization of self-alignment dynamics can be found in microswimmers, which are typically defined as micron-sized self-propelled entities in suspension in a solvent. These take their momentum from the surrounding fluid while conserving the total momentum. In such a situation, one may wonder whether the coupling of the translational and rotational degrees of freedom, which gives rise to self-alignment, will subsist. This question was already raised for the simplest case of asymmetrically patterned catalytic colloids, also called Janus colloids, in the seminal work by Anderson (1989).

Catalytic Janus colloids produce rapid motion in fluids by decomposing fuel asymmetrically around their body and taking advantage of the resulting gradients to develop motion through the corresponding phoretic flows. In principle, the asymmetric patterning of the colloidal particle can lead to a differential drag that produces a torque when the motion of the particle is not aligned with the polar axis of symmetry of the Janus pattern.

Considering a “slip-stick” spherical particle whose surface is partitioned into slip and no-slip regions, the coupling between torque and translation, as well as between force and rotation, can be obtained in the form of a Faxén-type formula in the limit where the slip length is small compared to the size of the particle (Swan and Khair, 2008; Premlata and Wei, 2021). This coupling, which is uncharacteristic of spherical particles in unbounded Stokes flow, originates purely from the slip-stick asymmetry and generically produces self-alignment. It is, however, likely that the difference of slip length between the two sides of a real Janus microswimmer is so small that in practice the coupling coefficient is also small. Nevertheless, the alignment with external forces was recently used to explain the chiral motion observed in light-activated Janus colloids (spherical silica particles half coated with carbon) that are moving in a viscoelastic fluid (Narinder, Bechinger, and Gomez-Solano, 2018). Finally, we mention that in some cases more complex interactions, including mutual torques such as the one produced between charge-induced dipole Janus colloids (Zhang *et al.*, 2021; Das *et al.*, 2024), could possibly map onto an effective self-aligning dynamics, thereby producing flocking or cluster phases.

## 3. Migrating cells

There is experimental evidence that epithelial-type cells on a substrate exhibit self-alignment properties at the collective level. Specifically, two of the main signatures of self-alignment, self-organized flocking in open boundary conditions (Szabó *et al.*, 2006; Malinverno *et al.*, 2017) and oscillations in confinement (Deforet *et al.*, 2014; Petrolli *et al.*, 2019; Peyret *et al.*, 2019), have been observed in epithelial cell sheets. An explicit biological role for self-alignment in the complex migration and deformation behavior of the simple sheetlike animal *Trichoplax* was also recently suggested (Bull, Prakash, and Prakash, 2021; Davidescu *et al.*, 2023).

Unlike in the case of mechanical agents, studying the active mechanics of cells in isolation is difficult, and emergent dynamical equations are only beginning to be proposed (Brückner *et al.*, 2022). There is, however, consensus that, at the single-cell level, a process called contact inhibition of locomotion (Abercrombie and Heaysman, 1954; Smeets *et al.*, 2016; Stramer and Mayor, 2017) slows and reorients cells when they encounter an obstacle. In fact, self-alignment with  $\mathbf{w} = \dot{\mathbf{v}}$ , in the linearized version, has been proposed as such a mechanism and explored explicitly in a 1D confining geometry (Camley and Rappel, 2014). In such a situation, the problem easily maps onto an effective equilibrium dynamics where the cell reverts polarization stochastically according to an Arrhenius-like process. Camley and Rappel extended their analysis to the case of multiple cells and showed that the increase in persistence time of a strongly confined cell and the interactions driving collective cell motility are intimately related to the self-aligning dynamics.

Single-cell dynamics is, however, of limited use to cells’ function in a tissue due to their transitioning from a mesenchymal migratory state [for example, the keratocytes discussed by Szabó *et al.* (2006)] to an densely packed epithelial state with a much different morphology. The latter is dominated by strong cell-cell junctions that incorporate both attractive-repulsive forces and active forces between cells, in addition to the individual active migration over the substrate (Alert and Trepak, 2020). Cell polarization as an internal state (called planar cell polarization in the biology community) is then variously defined as cell elongation, cell migration direction, actomyosin cortex polarization, or an anisotropy in chemical expression, with unclear distinctions among them (Ladoux and Mège, 2017). A number of competing feedback mechanisms related to activity that it is imperative to disentangle have been identified in cells. Separately, the plithotaxis mechanism (Tambe *et al.*, 2011) makes cells migrate along the direction of principal stress.

In the active matter community, hydrodynamic theories such as the active gel theory (Jülicher, Grill, and Salbreux, 2018) integrate this internal state information into a polarization vector, which in active nematics corresponds to the nematic orientation tensor (Doostmohammadi *et al.*, 2018), while motion is due to gradients in the stresses generated by the polarization. The hallmark of active nematic states are the appearance of motile  $\pm 1/2$  topological defects, which have been observed on average in epithelial cell sheets (Saw *et al.*, 2017). However, the connection between these stress gradients and the individual migration and feedback mechanisms

is unclear. Models that include nematic activity such as phase-field models (Doostmohammadi, Thampi, and Yeomans, 2016) and, more recently, vertex models (Rozman, Yeomans, and Sknepnek, 2023) have therefore been developed. Alternatively, such defect generation can also emerge from the interplay between nonaligning self-propulsion and deformability (Killeen, Bertrand, and Lee, 2022; Chiang *et al.*, 2024) and the observed mesoscopic “swirly” glasslike correlations in cell sheets (Angelini *et al.*, 2011) can also be understood in an active solid framework without any alignment (Henkes *et al.*, 2020).

Capturing these types of feedback has led to several computational cell models that include self-alignment, where cells are represented by network connections (Bull, Prakash, and Prakash, 2021; Davidescu *et al.*, 2023), particles (Szabó *et al.*, 2006; Smeets *et al.*, 2016), vertex models (Barton *et al.*, 2017; Malinverno *et al.*, 2017; Giavazzi *et al.*, 2018; Petrolle *et al.*, 2019), or phase-field models (Peyret *et al.*, 2019; Monfared *et al.*, 2023). We note that, given the strongly nonlinear internal dynamics of cells in response to external mechanical perturbations, the normalized  $\mathbf{w} = \hat{\mathbf{v}}$  velocity coupling has generally been used in these models.

#### IV. COLLECTIVE MOTION OF SELF-ALIGNING AGENTS

Collective motion is the hallmark of mutually aligning active agents. Yet, as discussed in the Introduction, collective motion does not arise only because of mutual alignment between the velocities of agents. In this context self-alignment models form a class of their own, with a distinct coupling between the translational and orientational degrees of freedom at the level of a single particle. We nevertheless later see that it also leads to collective motion under various circumstances.

##### A. Liquids of self-aligning agents

To our knowledge, the first work where self-alignment was introduced dates back to the early years of active matter (Shimoyama *et al.*, 1996). It was introduced in a model specifically designed to describe collective motion. The central ingredient of the model is to take into account the heading unit vector  $\hat{\mathbf{n}}$  and realize that in a glide, the heading and the velocity vector need not be parallel. The authors therefore assume that the heading relaxes to the direction of the velocity in a finite time. The dynamics of agent  $i$  was hence described by the following noiseless equations,

$$m\ddot{\mathbf{r}}_i = F_a\hat{\mathbf{n}}_i - \gamma\dot{\mathbf{r}}_i + \sum_{j \neq i} \alpha_{ij}\mathbf{f}_{ij} + \mathbf{g}_i, \quad (9a)$$

$$\tau_a\dot{\hat{\mathbf{n}}}_i = (\hat{\mathbf{n}}_i \times \hat{\mathbf{v}}_i) \times \hat{\mathbf{n}}_i, \quad (9b)$$

corresponding to Eq. (4), in the case with  $\mathbf{w} = \hat{\mathbf{v}}$  and an isotropic translational damping. The forces acting on the particles are the pairwise interaction forces  $\alpha_{ij}\mathbf{f}_{ij}$ , which in this case are not necessarily isotropic, and a global cohesive force  $\mathbf{g}_i$ . The interaction forces and this global cohesive force share the same amplitude  $c$ .

After rescaling the length by the interaction range  $r_c$  and the time by  $\tilde{t}_0 = r_c/v_a$ , where  $v_a = F_a/\gamma$  is the steady-state active

speed of a free agent, Shimoyama *et al.* (1996) introduced three dimensionless parameters:  $P = \gamma r_c/\tau_a F_a$ ,  $R = mF_a/\gamma^2 r_c$ , and  $Q = F_a/c$ . Here  $P$  is the ratio between the interaction time  $r_c\gamma/F_a$  and the alignment time  $\tau_a$  of the orientation,  $R$  is the inertia to damping ratio, and  $Q$  is the active-force-to-interaction-force ratio. Shimoyama *et al.* considered the overdamped regime where  $R \ll 1$  and reported a transition from disordered dynamics to collective motion controlled by the ratio  $G = P/Q$ : at large  $G$  the dynamics are chaotic and analogous to the swarming of mosquitos; at small  $G$  the dynamics are highly polarized and analogous to the marching of cranes. In the transitional regime, the collective motion is wandering, in a way akin to the motion of sparrows; see Fig. 3(a). The influence of noise is not reported.

Ten years passed before a similar model including self-alignment was introduced by Szabó *et al.* (2006) to describe the collective migration of tissue cells. They modeled an  $i$ th cell by a disk-shaped particle whose position  $\mathbf{r}_i$  and orientation  $\hat{\mathbf{n}}_i = (\cos \theta_i, \sin \theta_i)$  evolve in a 2D plane following the overdamped equation of motion

$$\dot{\mathbf{r}}_i = v_0\hat{\mathbf{n}}_i + \alpha \sum_{j=1}^N \mathbf{F}_{ij}, \quad (10a)$$

$$\dot{\theta}_i = \frac{1}{\tau_a} \sin^{-1}[(\hat{\mathbf{n}}_i \times \hat{\mathbf{v}}_i) \cdot \hat{e}_z] + \sqrt{2D_\theta} \eta_i, \quad (10b)$$

where  $\hat{e}_z$  is a unit vector orthogonal to the plane of motion and  $\eta_i$  is a random variable that introduces  $\delta$ -correlated Gaussian white noise with zero mean, i.e., with  $\langle \eta_i(t) \rangle = 0$  and  $\langle \eta_i(t)\eta_j(t') \rangle = \delta_{ij}\delta(t-t')$ . Equation (10a) is the overdamped version of Eq. (2), with  $v_0 = F_a/\gamma$ . The interaction forces are short-range and contain a repulsive part, an attractive part, and an adhesive part; see Szabó *et al.* (2006) for an exact expression. Equation (10b) can be recast in a simpler form as

$$\dot{\theta}_i = \frac{1}{\tau_a}(\psi_i - \theta_i) + \sqrt{2D_\theta} \eta_i, \quad (11)$$

where  $\psi_i$  denotes the orientation of the velocity,  $\hat{\mathbf{v}}_i = (\cos \psi_i, \sin \psi_i)$ . It thus amounts to a linearization of the overdamped version of Eq. (5b) in the  $\mathbf{w} = \hat{\mathbf{v}}$  case.

In contrast to the model proposed by Shimoyama *et al.*, this model incorporates angular noise but does not include long-range global forces. The resulting dynamics exhibit a continuous transition from a disordered to an ordered state, which can be achieved by reducing noise or increasing density; see Fig. 3(b). The model was also used to examine the impact of confinement, revealing the emergence of circular motion across a wide range of parameters, which is consistent with experimental observations of cellular behavior.

Self-alignment was first experimentally identified when it was found to be the root cause of the onset of the collective motion observed in a system of vibrated polar disks (Deseigne, Dauchot, and Chaté, 2010; Deseigne *et al.*, 2012). In this setup millimeter-sized objects were designed to be self-propelled agents that advance along a well-defined axis when placed on a vibrating surface while remaining disk shaped with respect to collisions and thus interacting with

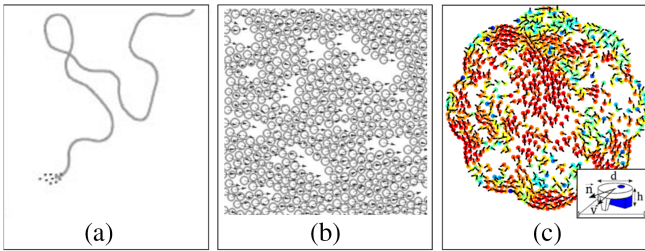


FIG. 3. Collective motion in self-aligning liquids. (a) Early simulations in the first model of self-aligning agents. Adapted from Shimoyama *et al.*, 1996. (b) Simulations in a large population of self-propelled self-aligning cells, modeled as disk-shaped particles. Adapted from Szabó *et al.*, 2006. (c) Experimental evidence of collective motion in a system of vibrated polar disk-shaped grains. The particles' colors indicate the degree of local alignment between particles: perfect alignment, red and perfect antialignment, blue. The intrinsic polarity of the particles is indicated by the black arrows. Adapted from Deseigne, Dauchot, and Chaté, 2010.

neighbors through central, isotropic forces; see Fig. 3(c). Weber *et al.* (2013) developed a faithful model for the motion, collisions, and self-alignment of such polar disks in order to extend their experimental observations to larger *in silico* systems. The model that they introduced reads

$$m\ddot{\mathbf{r}}_i = F_a \hat{\mathbf{n}}_i - \gamma \dot{\mathbf{r}}_i + \sum_{j \neq i} \mathbf{f}_{ij} + \eta_i^{\parallel} \hat{\mathbf{n}}_i + \eta_i^{\perp} \hat{\mathbf{n}}_i^{\perp}, \quad (12a)$$

$$\dot{\theta}_i = \beta \text{sign}[\cos(\psi_i - \theta_i)] \sin(\psi_i - \theta_i), \quad (12b)$$

with a self-alignment of  $\hat{\mathbf{n}}$  toward  $\hat{\mathbf{v}}$ . The agents interact via inelastic collisions encoded in the pairwise forces  $\mathbf{f}_{ij}$ . The damping is isotropic but the “active noise” is anisotropic, respecting the particle’s polar symmetry: the random variables  $\eta_i^{\parallel, \perp}$  follow a Gaussian distributed white noise with zero mean, i.e.,  $\langle \eta_i^{\parallel, \perp}(t) \eta_j^{\parallel, \perp}(t') \rangle = 2D_{\parallel, \perp} \delta_{ij} \delta_{\parallel, \perp} \delta(t - t')$ , where  $D_{\parallel, \perp}$  is the corresponding diffusion constant. There is no noise on the angular dynamics. One interesting specificity of this model is that the sign of the coupling changes according to  $\alpha_i = \angle(\mathbf{v}_i, \hat{\mathbf{n}}_i) = \theta_i - \psi_i$ , the angle between velocity and polarity. For  $|\alpha_i| > \pi/2$  it was assumed that frictional interactions with the vibrating plate would rotate  $\hat{\mathbf{n}}_i$  toward  $\mathbf{v}_i$ , producing self-alignment, while for  $|\alpha_i| > \pi/2$  it was assumed that  $\hat{\mathbf{n}}_i$  would instead rotate toward  $-\mathbf{v}_i$ . To our knowledge, this is one of only two examples in the literature where what could be called a nematic self-alignment was introduced. The other one, in the nematic flocks on spheres of Henkes, Marchetti, and Sknepnek (2018), supplements more traditional nematic pair alignment, and is necessary to produce the torques that generate  $\pm 1/2$  defects.

By calibrating the model parameters using experimental data from the single-particle dynamics and collision statistics, Henkes, Marchetti, and Sknepnek were able to obtain quantitative agreement between the experiments and the model also at the collective level. From there they could show firm numerical proof of the transition to collective motion in this system. Note that a simpler form of self-alignment of  $\hat{\mathbf{n}}$  toward

$\mathbf{v}$ , regardless of  $\alpha_i$ , also promotes the transition to collective motion, as later demonstrated by Lam, Schindler, and Dauchot (2015a) and Lam, Schindler, and Dauchot (2015b). Given the isotropic pairwise interactions of the disks, this result underlines the notion that collective motion can emerge from self-alignment alone. It is thus tempting to think of self-alignment as one specific microscopic mechanism (among others) that can lead to a form of effective pairwise mutual alignment, which would thereby belong to the class of active matter systems described by the Vicsek model (Vicsek *et al.*, 1995).

However, the situation is not that simple, as demonstrated by Lam, Schindler, and Dauchot (2015a, 2015b), where the Landau terms of the large-scale hydrodynamics were derived for a system of self-propelled hard disks obeying self-alignment in the  $\mathbf{w} = \mathbf{v}$  case. They adopted the same units and timescales as Shimoyama *et al.* (1996), with  $r_c$  the diameter of the hard disks, and wrote the dimensionless equation of motion as

$$\tilde{\tau}_v \ddot{\mathbf{r}} = \hat{\mathbf{n}} - \dot{\mathbf{r}} + \sum_{j \neq i} \mathbf{f}_{ij}, \quad (13a)$$

$$\tilde{\tau}_n \dot{\hat{\mathbf{n}}} = (\hat{\mathbf{n}} \times \dot{\mathbf{r}}) \times \hat{\mathbf{n}} + \sqrt{2D_r} \eta \hat{\mathbf{n}}^{\perp}, \quad (13b)$$

with  $\tilde{\tau}_v = mF_a/\gamma^2 r_c$  and  $\tilde{\tau}_n = 1/\beta r_c = l_a/r_c$ . When two particles obeying the aforementioned dynamics collide, even elastically, the polarities of the particles and their respective velocities strongly misalign. This leads to a relaxation process during which the polarity and the velocity rotate toward each other until  $\mathbf{v}_i = \hat{\mathbf{n}}_i$ . Each collision followed by this relaxation process was named a scattering event. For symmetric collisions it is easy to see that such scattering events will induce an alignment of the velocities of the two particles.

Using these equations and integrating over all possible pairwise events, Lam, Schindler, and Dauchot (2015a, 2015b) computed the effective total pairwise alignment strength as a function of the incoming angle of the collisions and thereby obtained the mean-field phase diagram of the model in the low-density limit; see Fig. 4(a). In the absence of noise, a strongly discontinuous transition from the disordered state to a highly polar liquid, or the flocking state, takes place when the ratio  $\alpha = \tilde{\tau}_n/\tilde{\tau}_v$  exceeds a critical value  $\alpha^*(\rho)$  that decreases with the density  $\rho$ . If we add noise, the transition shifts to higher values of  $\alpha$  and, for large enough noise, it becomes continuous. For a finite value of the noise, there is a reentrant transition toward the disordered state when  $\alpha$  becomes too large. This can be understood intuitively as follows. When  $\alpha$  is small, the relaxation of the polarization toward the velocity is so fast that self-alignment does not affect the orientation of the velocity and the liquid remains disordered. When  $\alpha$  is too large, the persistence of  $\hat{\mathbf{n}}$  is so large that it is not influenced by the collisions with other agents; mutual alignment cannot set in and the liquid remains disordered. The phase diagram displayed on Fig. 4(a) is obtained in the limit of large  $\tilde{\tau}_v$ . When  $\tilde{\tau}_v$  is decreased, the left boundary of the flocking region remains unchanged, while the right one shifts toward larger  $\alpha$ .

An important point made by Lam, Schindler, and Dauchot (2015a, 2015b) is that the dependence of the effective alignment strength on the incoming angle of the collision is

markedly different from the one obtained from the Vicsek aligning rules. A qualitative consequence of this difference is that the mean-field transition to collective motion is second order in the case of the Vicsek model, while we saw that its order depends on the amplitude of the noise in the case of self-aligning hard disks. Whether this qualitative difference observed at the mean-field level has significant impact on the transition with spatial fluctuations remains an open issue that is notoriously difficult to address because the nucleation process leading to collective motion takes place at a bimodal line far away from the spinodal line.

Except for the presence of cohesion discussed by Shimoyama *et al.* (1996), the deterministic dynamics introduced in this review and by Lam, Schindler, and Dauchot (2015b) are essentially the same. Their results are complementary in the sense that they explore two different limits. Indeed, if we compare Eqs. (9) and (13), we see that  $\tilde{\tau}_v = R$  and  $\tilde{\tau}_n = P^{-1}$ . While Shimoyama *et al.* (1996) considered the overdamped limit  $R \rightarrow 0$ , Lam, Schindler, and Dauchot (2015b) studied the hard disk limit  $Q \rightarrow 0$ . Together they established that, in the absence of noise, the mean-field transition to collective motion takes place for  $\tilde{\tau}_n > \tilde{\tau}_n^*(\tilde{\tau}_v, Q)$ , with

$$\tilde{\tau}_n^*(\tilde{\tau}_v \rightarrow 0, Q) \sim Q^{-1}, \quad (14a)$$

$$\tilde{\tau}_n^*(\tilde{\tau}_v, Q \rightarrow 0) \sim \tilde{\tau}_v. \quad (14b)$$

Most models of self-propelled particles are considered in the overdamped limit ( $\tilde{\tau}_v \rightarrow 0$ ). Softer potential than the strictly hard disk interaction discussed by Lam, Schindler, and Dauchot (2015b) is then also studied. For such overdamped models, we have  $\mathbf{v}_i = \hat{\mathbf{n}}_i$  and no self-aligning term at all times, except for the duration  $\tau_i$  of the interaction, during which the self-alignment will reorient the  $\mathbf{v}_i$  velocities. According to the analysis of Lam, Schindler, and Dauchot (2015a), what matters is the persistence of the polarization throughout the scattering event. It is thus the ratio  $\tilde{\tau}_n/\tau_i$  that plays the role of the aforementioned parameter  $\alpha$ . The transition reported by Szabó *et al.* (2006) is mean-field-like because of the small system size that are considered. Its continuous nature can thus be understood, in light of the earlier discussion, as a transition taking place for large enough  $\tilde{\tau}_n/\tau_i$ .

When the density becomes so large that crowding effects become significant, equilibrium liquids experience a strong increase of their viscosity, eventually reaching the glass transition when crystallization is avoided. The interplay of activity and glassiness has attracted significant attention (Janssen, 2019). However, most studies have not considered the presence of alignment, and even less so the presence of self-alignment, except for the recent work of Paoluzzi, Levis, and Pagonabarraga (2024), who studied a polydisperse system of particles with self-aligning dynamics described by

$$\dot{\mathbf{r}}_i = v_0 \hat{\mathbf{n}}_i + \mu \mathbf{F}_i, \quad (15a)$$

$$\dot{\theta}_i = \beta \sin(\psi_i - \theta_i) + \sqrt{2D_r} \eta_i, \quad (15b)$$

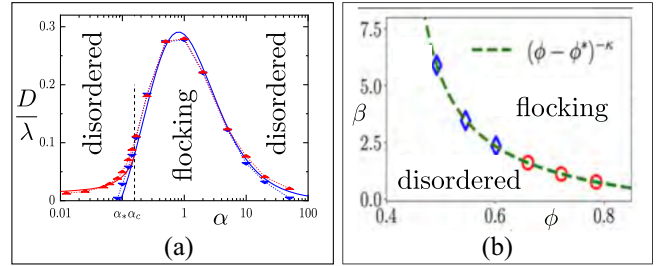


FIG. 4. Phase diagrams for collective motion in liquids composed of self-aligning particles. (a) Diagram obtained numerically (blue and red data points) from the simulations of Eqs. (13a) and (13b) with density  $\rho = 10^{-2}$  and analytically in the limit of low densities and  $\tilde{\tau}_v \rightarrow \infty$  (black line). The blue (red) data points denote the location of the transition when  $\alpha$  is increased (decreased). For  $\alpha > \alpha_c$  the two datasets merge and the transition is continuous; for  $\alpha < \alpha_c$  it is discontinuous.  $D/\lambda$  denotes the ratio of the angular noise amplitude to the collision rate and  $\alpha = \tilde{\tau}_n/\tilde{\tau}_v$ . Adapted from Lam, Schindler, and Dauchot, 2015b. (b) Diagram obtained numerically from the simulations of Eqs. (10a) and (10b). At large packing fractions (red markers), the transition is continuous; at small packing fraction (blue markers), it is discontinuous. Adapted from Paoluzzi, Levis, and Pagonabarraga, 2024.

where  $\psi_i$  is the direction of  $\hat{\mathbf{v}}_i$ . The dynamics in this case is overdamped, as in the work of Szabó *et al.* (2006), but the self-aligning term is not linearized in  $\psi_i - \theta_i$ .

Szabó *et al.* reported that a transition to collective motion takes place when  $\beta$  exceeds a density dependent threshold  $\beta^*(\phi)$ . Within the limit of their finite-size simulations, they observe that the transition is first order at moderate values of  $\phi$ , while it becomes second order for large  $\phi$  [Fig. 4(b)] and remains second order when the system size is increased.

For smaller self-alignment Szabó *et al.* (2006) observed the well-known MIPS, which takes place at large enough densities in systems of nonaligning repulsive active Brownian particles (Cates and Tailleur, 2015). This transition appears to be mutually exclusive with the transition to collective motion. At higher densities the system instead reaches a glassy state where the relative motion of particles ceases. Nevertheless, the flocking transition is not suppressed in this regime, and Szabó *et al.* distinguished “glassy” from “flocking glass” states.

## B. Collective motion in a confining potential

Recently, the collective dynamics of self-aligning polar active matter, interacting repulsively through a truncated Lennard-Jones potential and confined in a harmonic potential, were investigated numerically by Canavello *et al.* (2024). In their work the particles obey the overdamped dynamics described by Eq. (5) in the case with  $\mathbf{w} = \mathbf{v}$ .

The main output of their work was a phase diagram and a description of the dynamical phases, as summarized in Fig. 5. In the small  $\beta$  and large noise  $D$  region, all polar order parameters vanish, which characterizes the unpolarized or paramagnetic state. Decreasing  $D$  while maintaining a small  $\beta$ , here typically smaller than 1, the dynamics enters the radially polarized (RP) state displayed in Fig. 5(a), where all particles point outward. Increasing  $\beta$  while keeping  $D$  small, the system organizes into a vortex state, first in a shear banded vortex

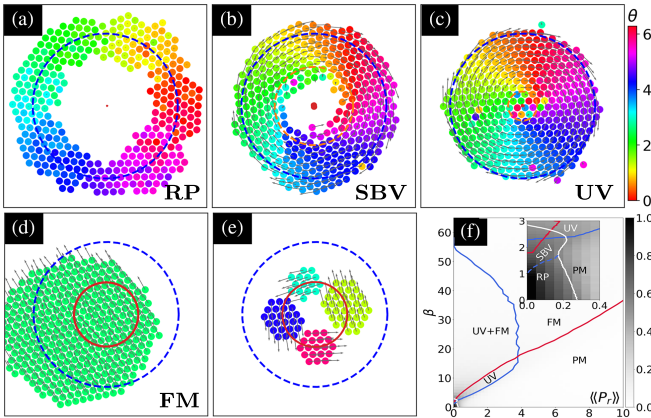


FIG. 5. Collective motion in a harmonic potential. The main dynamical states observed, when varying the self-aligning strength  $\beta$  and the rotational noise  $D$ , are displayed with the color coding for the orientation of the particle. (a) Radially polarized (RP) state. (b) Shear banded vortex (SBV) state. (c) Uniform vortex (UV) state. (d) Orbiting ferromagnetic (FM) state. (e) Multiorbiting polar cluster state observed at lower packing fraction. (f) Phase diagram in the  $\beta$ - $D$  plane. Inset: enlargement of the small  $\beta$ , small  $D$  region. The gray intensity shows the time-averaged radial polarization  $\langle P_r \rangle$ . Adapted from [Canavello \*et al.\*, 2024](#).

(SBV) state shown in Fig. 5(b), which rapidly turns into the uniform vortex (UV) state in Fig. 5(c) for large enough  $\beta$ . This uniform vortex does not rotate as a strict rigid body but rather as a deformable solid. Increasing  $\beta$  at large noise, the system adopts a ferromagnetic (FM) state where a polarized cluster revolves without rotation; see Fig. 5(d). When the packing fraction is low, this unique cluster may break into several smaller clusters; see Fig. 5(e).

[Canavello \*et al.\* \(2024\)](#) also reported that the orbiting ferromagnetic phase is highly resilient to noise, as it is stable even at high values of  $D$ , especially for high angular mobility, while the uniform vortex phase is typically much more sensitive to fluctuations. As shown in the phase diagram [Fig. 5(f)], the uniform vortex and the ferromagnetic states coexist for low enough noise. As a result, the transition from the uniform vortex state to the ferromagnetic one and back exhibits a pronounced hysteretic behavior.

### C. Collective motion in active Voronoi models

Epithelial cell sheets are confluent monolayers of active cells where individual cells interact both with a substrate and with other cells in an arrangement that resembles cobblestone pavement; see Fig. 6(a). To model this geometry, the vertex model of epithelial cell sheets ([Nagai and Honda, 2001](#); [Farhadifar \*et al.\*, 2007](#)) maps them to a planar polygonal tiling in which cell shapes were initially determined by energy minimization as in foam models; see [Fletcher \*et al.\* \(2014\)](#) for a review. In the now consensus energy functional

$$V_{\text{vertex}} = \sum_{i=1}^N \frac{\kappa}{2} (A_i - A_0)^2 + \frac{\Gamma}{2} (P_i - P_0)^2, \quad (16)$$

the shape of each cell is constrained by an area stiffness  $\kappa$  that constrains fluctuations away from a target area  $A_0$  and a

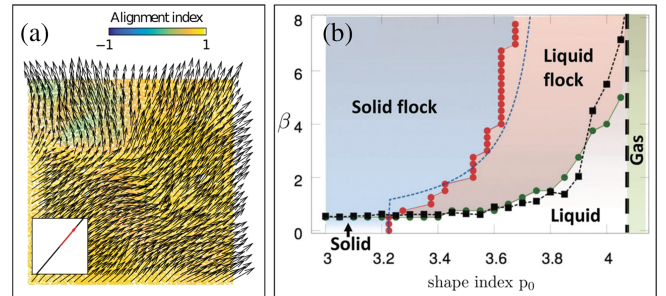


FIG. 6. Epithelial tissues and active Voronoi models. (a) Human mammary epithelial cells treated with RAB5A-MCF-10A and inducing flocking motion. The velocity field is obtained from particle image velocimetry (PIV). The red arrow in the inset is the mean velocity  $\mathbf{v}_0$  (averaged over the entire field of view). The color map reflects the alignment with respect to the mean velocity as quantified by the alignment index. Adapted from [Malinverno \*et al.\*, 2017](#). (b) Alignment-shaped index phase diagram as obtained from a self-propelled Voronoi model with self-alignment. The native SPV model corresponds to the horizontal axis, with  $\beta = 0$ . Adapted from [Giavazzi \*et al.\*, 2018](#).

perimeter stiffness  $\Gamma$  that likewise constrains perimeter fluctuations. This energy is expressed as a function of the vertex positions  $\mathbf{r}_\mu$  of the cell polygonal shapes.

To make the previous model active, [Bi \*et al.\* \(2016\)](#) incorporated cell crawling motility over a substrate by introducing overdamped Langevin dynamics akin to active Brownian motion,

$$\dot{\mathbf{r}}_i = v_0 \hat{\mathbf{n}}_i - \alpha \nabla_i V_{\text{vertex}}, \\ \dot{\theta}_i = \sqrt{2D_\theta} \eta_i.$$

While this dynamics is conceptually straightforward, the presence of the gradient with respect to the cell center positions  $\mathbf{r}_i$  requires a one-to-one continuously differentiable map between these and the vertex positions  $\mathbf{r}_\mu$ . This can be solved using the dual between a Delaunay triangulation among cell centers and a Voronoi tiling for the vertex positions, which led to the adoption of the name self-propelled Voronoi (SPV) model. The SPV model admits two phase transitions between a rigid solid state and a liquid state [Fig. 6(b): one when cell motility  $v_0$  becomes large enough and the other when cells have a more elongated shape, as quantified by the shape index  $p_0 = \sqrt{P_0}/A_0$ . This index measures the preferred perimeter relative to the preferred area, with the system being liquid (for  $v_0 = 0$ ) if  $p_0$  is above a critical  $p_0^* \approx 3.81$  ([Park \*et al.\*, 2015](#)).

The native SPV model can be enriched with self-alignment in the form of an explicit alignment torque ([Barton \*et al.\*, 2017](#)),

$$\dot{\mathbf{r}} = v_0 \hat{\mathbf{n}}_i - \alpha \nabla_i V_{\text{vertex}}, \quad (17)$$

$$\gamma_r \dot{\theta}_i = \boldsymbol{\tau}_i \cdot \hat{\mathbf{z}} + \sqrt{2D_\theta} \eta_i, \quad \boldsymbol{\tau}_i = J_v (\hat{\mathbf{n}}_i \times \hat{\mathbf{v}}_i) \times \hat{\mathbf{n}}_i, \quad (18)$$

where  $\hat{\mathbf{z}}$  is the out-of-plane unit vector. This model produces a flocking state at sufficiently strong alignment  $\beta = J_v/\gamma_r$ . It

was used to investigate the flocking transition in cell sheets by [Malinverno \*et al.\* \(2017\)](#) and [Giavazzi \*et al.\* \(2018\)](#).

More specifically, [Malinverno \*et al.\* \(2017\)](#) developed an experimental system of human mammary epithelial cells. In its natural state, this cell sheet acts as a liquid with spatiotemporally correlated motion, but without global flocking. Treating it with RAB5A-MCF-10A, which weakens the intercellular adhesive bonds, has been empirically shown to induce a transition to flocking motion in the sheet; see Fig. 6(a). Including velocity self-alignment, as previously introduced for the dynamics, recovers this transition, now as a function of  $J_v$ . Separately, [Giavazzi \*et al.\* \(2018\)](#) mapped the full phase space of this model as a function of the shape parameter  $p_0$  and the alignment strength  $\beta = J_v/\gamma_r$  for constant active driving and rotational noise; see Fig. 6(b). As in the particle-based case, this model admits both a solid-to-liquid transition and a flocking transition, including a solid flocking phase. The precise nature of these transitions and of the flocking phase have not yet been explored in detail.

#### D. Collective motion in a crystal of self-aligning disks

If we consider high densities, the kinetic theory calculation that demonstrates the emergence of collective motion in a dilute assembly of self-aligning hard disks is not supposed to hold ([Lam, Schindler, and Dauchot, 2015a](#)). This is all the more true when the time separating two collisions becomes shorter than the relaxation times of the polarity and velocity. One would thus expect collective motion to be preempted by crowding effects at large densities. Surprisingly, this is not the case, as demonstrated by [Briand and Dauchot \(2016\)](#) and [Briand, Schindler, and Dauchot \(2018\)](#), who investigated both experimentally and numerically dense assemblies of monodisperse self-aligning hard disks. They found two emerging effects of the active self-aligning dynamics.

First, the crystallization transition obeys a scenario that is radically different from the equilibrium case. The transition toward the crystal phase is marked by the emergence of close-packed crystallites, which coexist with a surrounding moving fluid. Increasing the density, the crystallites merge into a large hexatic phase populated with strongly dynamical defects, leading to a complete decoupling of the dynamics and the structure. While the structure is dominated by that of a close-packed crystal, the mean-square displacement exhibits no plateau and remains superdiffusive on long timescales. There is no truly slow dynamical regime, and all particles rearrange their position with respect to their neighbors on a modest timescale.

Second, and more surprisingly, the authors [Briand and Dauchot \(2016\)](#) and [Briand, Schindler, and Dauchot \(2018\)](#) reported the existence of a flowing crystalline phase. After a long transient, a perfect crystalline lattice with initially random orientation of the polarities starts moving as a whole with all particles aligned in the same direction: despite the high-frequency collisions, self-alignment still produces collective motion. When the crystal is prepared in a hexagonal arena that respects the same crystalline symmetry, the entire system spontaneously forms a macroscopic sheared flow while conserving an overall crystalline structure; see Fig. 7. This flowing crystalline structure, which was called a

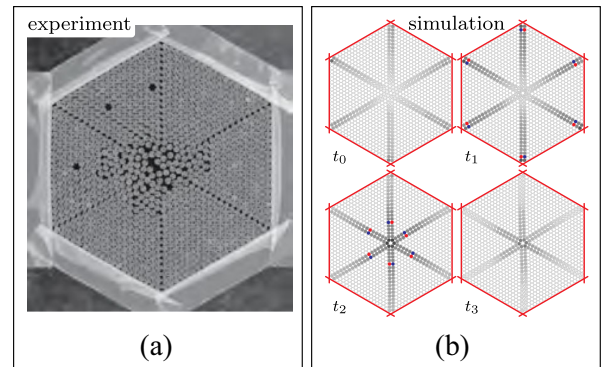


FIG. 7. Collective motion in a crystal of self-aligning disks. (a) Image of a dense packing of self-propelled vibrated disks (packing fraction  $\phi = 0.86$ ) confined in a hexagonal arena that forms a self-flowing crystal, with shear localization along default lines emerging from the corner of the hexagon and merging in its center. Adapted from [Briand, Schindler, and Dauchot, 2018](#). (b) Simulation of the same system at low noise and even higher packing fraction ( $\phi = 0.88$ ), which produces the same phenomenology with an even higher level of order in both space and time. Adapted from [Briand, Schindler, and Dauchot, 2018](#).

rheocrystal, is made possible by the condensation of shear along localized stacking faults. In the presence of noise, the core of the system concentrates the defects and remains disordered; see Fig. 7(a). Note the strong similarities between this flowing crystal and the uniform vortex state reported in Fig. 5(c). Performing simulations for larger system sizes, with an experimentally realistic packing fraction and noise level, the disordered core was observed to occupy a smaller fraction of the system, while the flowing velocity slowly converged to a higher value. Numerically, it is also possible to reduce the noise and increase the packing fraction to a point where the structure is defect-free in the core and the dynamics eventually becomes periodic in time; see Fig. 7(b). The highest packing fraction for which the crystal flows is controlled by the fraction of space needed for the stacking faults to take place. Since the latter is subextensive, the flowing crystal phase range enlarges with increasing system size.

#### E. Collective motion of active elastic sheets

Motivated by experiments performed with wheeled robots ([Ferrante \*et al.\*, 2012](#); [Brambilla \*et al.\*, 2013](#)) [Ferrante \*et al.\* \(2013a, 2013b\)](#) introduced an active elastic sheet model to describe groups of self-propelled agents moving on an arena while linked by linear springlike attraction-repulsion interactions. These agents obey the following overdamped equations of motion:

$$\dot{\mathbf{r}}_i = v_0 \hat{\mathbf{n}}_i + \alpha_{\parallel} [(\mathbf{F}_i + \tilde{D}_r \hat{\xi}_i^r) \cdot \hat{\mathbf{n}}_i] \hat{\mathbf{n}}_i, \quad (19a)$$

$$\dot{\theta}_i = \beta_\theta [(\mathbf{F}_i + \tilde{D}_r \hat{\xi}_i^r) \cdot \hat{\mathbf{n}}_i^\perp] + \tilde{D}_\theta \eta_i. \quad (19b)$$

Noise was introduced in the headings and in the virtual interaction forces (corresponding to actuation and sensing noise in the context of robotics) by adding the random variables  $\eta_i$  (a  $\delta$ -correlated scalar with zero mean Gaussian white noise

distribution, as previously discussed) and  $\hat{\xi}_i^r$  (a  $\delta$ -correlated randomly oriented unit vector), with amplitudes  $\tilde{D}_\theta$  and  $\tilde{D}_r$ , respectively. The total forces over agent  $i$  are evaluated as  $\mathbf{F}_i = \sum_{j \in S_i} (-k/l_{ij})(|\mathbf{r}_{ij}| - l_{ij})\mathbf{r}_{ij}/|\mathbf{r}_{ij}|$ , where  $k/l_{ij}$  is the spring constant,  $\mathbf{r}_{ij} = \mathbf{r}_j - \mathbf{r}_i$ , and  $l_{ij}$  is the equilibrium distance between the interacting agents  $i$  and  $j$ . Note that the interactions are permanent in this setting, so the interaction network remains unchanged throughout the dynamics. By connecting nearest neighbors on a plane, we thus define a structure that can be viewed as an active elastic sheet.

A unique feature of this model is that the mobility tensor  $\alpha = \gamma^{-1}$  is fully anisotropic, with zero mobility along  $\hat{\mathbf{n}}_i^\perp$  and  $\alpha_\parallel$  mobility along  $\hat{\mathbf{n}}_i$ . It thus describes agents that cannot translate in the  $\hat{\mathbf{n}}_i^\perp$  direction, because this would correspond to the wheeled robots sliding sideways. Correspondingly, as described in Sec. III.C.1, the angular dynamics does not result strictly from self-alignment and is instead equivalent to torques introduced by off-centered elastic forces, where  $\beta_\theta$  results from the combined effect of the lever arm and the rotational mobility. Note, however, that this equivalence is not complete, since the forces  $\mathbf{F}_i$  in this model are computed from center to center, an artifact introduced to avoid the need for sensing other robots' headings.

An elastic sheet of linked nearest neighbors following these dynamics self-organizes into a polarized state with common headings despite having no explicit alignment forces (Ferrante *et al.*, 2013b). A numerical finite-size scaling analysis also showed long-range order at nonzero noise, in an apparent contradiction with the Mermin-Wagner theorem (Mermin, 1968) and in contrast to Vicsek-like models with fixed interaction networks (Vicsek and Zafeiris, 2012). It was argued that this is because the self-organizing mechanism here is fundamentally different, based on the focusing of self-propulsion energy into lower elastic modes rather than on explicit local alignment. This model was implemented as a control algorithm in experiments with wheeled robots (e-pucks) by Zheng, Huepe, and Han (2020), who showed that self-organized collective translation or rotation were reached for a broad range of parameters, despite multiple real-world limitations such as communication delays; see Fig. 8(a). However, these ordered states presented marginal linear stability and thus displayed persistent oscillations. Other studies have considered 1D chains of elastically linked self-aligning active agents instead of 2D elastic sheets, showing interesting collective dynamics in simulations (Ferrante *et al.*, 2013b; Teixeira, Fernandes, and Brunet, 2021).

The same model was used to explore a potential alternative explanation for the scale-free correlations measured in bird flocks (Huepe *et al.*, 2015), which have been argued to result from their critical state (Cavagna and Giardina, 2014). It was suggested that the attraction-repulsion forces between birds produce an elasticlike coupling between active agents, exciting low elastic modes that trivially scale with the size of the system. A similar argument was provided in an equilibrium model of self-aligning rotors (Casiulis *et al.*, 2020).

Turgut *et al.* (2020) exploited the permanent nature of the interaction between agents in this model to compare the resilience of the aligned state to noise for nontrivial interaction networks, where elastic connections are established between

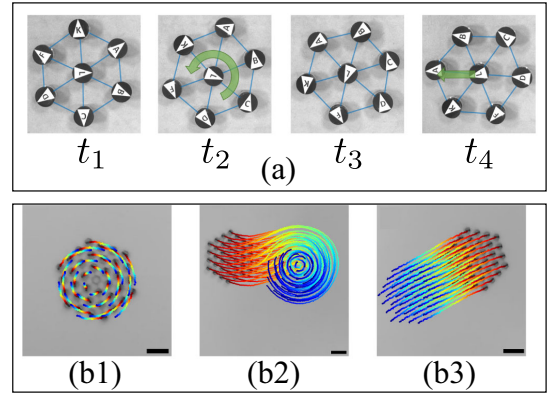


FIG. 8. Collective motion in active elastic sheets. (a) Successive snapshots of a robot swarm experiment that implements the position-based decentralized control algorithm based on Eq. (B7) and realizes translating collective motion ( $t = t_4$ ) after sometimes visiting a metastable rotational state (here  $t = t_2$ ). The overlaid blue lines indicate which robots are interacting. Adapted from Zheng, Huepe, and Han, 2020. (b) Active elastic structures obtained by physically connecting active units with springs [see Sec. V.A and Fig. 9(b)] perform spontaneous solid body rotation (left image) and translation (right image), with the rotation being metastable with respect to translation (center image). Adapted from Hernández-López *et al.*, 2024.

agents beyond the nearest neighbors. They showed that if we fix the mean number of interactions per agent, the critical noise will always increase as more random (long-range) links with Erdős-Rényi connectivity replace nearest neighbor interactions but will instead reach a maximum and then decrease if these random links have a scale-free degree distribution (Newman, 2010). Therefore, in contrast to most cases in network science, here the scale-free topology does not favor system integration.

The model was also recently extended (Lin, Han, and Huepe, 2021) to describe a mechanical representation of an elastic sheet composed of self-propelled agents linked through linear springs attached to the tip of forward-projecting lever arms of length  $R$ . This version of the model also uses Eqs. (19) but redefines the relative position with respect to which the forces are measured as the vector between the tips of the lever arms of the agents (where the physical springs would actually be attached), given by  $\mathbf{r}_{ij} = (\mathbf{r}_j + R\hat{\mathbf{n}}_j) - (\mathbf{r}_i + R\hat{\mathbf{n}}_i)$ , instead of between the agent centers. For small  $R/l_{ij}$ , the interaction thus depends mainly on relative positions, not on relative angles, and the resulting states display the same features as in the original model. For large  $R/l_{ij}$  the interactions strongly depend on changes in the relative angles and become akin to the ferromagneticlike alignment in the Vicsek model, displaying equivalent stationary states, including a loss of order for large enough systems at intermediate noise levels due to the Mermin-Wagner effect. For an intermediate range of parameters, the system can transition to a novel state of quenched disorder with random fixed mean headings. This state was described analytically by Lin *et al.* (2023) for an analogous case with only repulsive interactions that is akin to a dense system of self-propelled polar disks with off-centered rotation. The latter system of disks was recently studied

numerically under circular confinement by Tang *et al.* (2024), showing the coexistence of collective states driven by self-alignment and mutual alignment.

Finally, we note that the dynamics of a wheeled robot model with fully anisotropic mobility tensor, as described by Eqs. (19), has to be inherently elastic. Indeed, the strong constraint imposed by the mobility tensor would make it a singular model in the limit where the active agents are connected by stiff springs. This singularity is removed when we relax this anisotropy and allow the agents to glide sideways. In this rigid limit, if we consider an isotropic mobility tensor, stress propagation alone induces self-organization without exciting the vibrational modes. In the limit of rigid bonds, a mean-field-like transition is observed due to the truly long-range interaction between agents. In this limit a general Landau-like formalism can be established to understand the dynamics of collective motion along different floppy modes in such structures ranging from rigid body motion to folding mechanisms (Hernández-López *et al.*, 2024).

## V. COLLECTIVE ACTUATION OF ACTIVE ELASTIC MATERIALS

Because self-alignment is not only effective pairwise alignment but also alignment on the force field, one can expect interesting new dynamics to emerge when self-aligning polar agents are embedded in an elastic material attached to a frame. On the one hand, the positional degrees of freedom of the active agents have a well-defined reference state. On the other hand, activity endows them with an additional degree of freedom in the form of polar active forces. These forces are expected to deform the elastic matrix and induce a stress strain field that depends on the forces' configuration, that is, on the agents' positions and orientations. The strain or stress tensor may in turn reorient the forces. This generic nonlinear elastoactive feedback opens the path toward spontaneous collective excitations of the solid, which were named collective actuation by Baconnier *et al.* (2022). In the following we start by describing collective actuation in a paradigmatic model experimental system composed of active elastic structures. We then report the apparent observation of collective actuation in jammed systems of particles and in active Voronoi models in confinement. Finally, we discuss the observation of similar dynamical behaviors in various biological systems.

### A. Selective and collective actuation in elastic lattices

A minimal experimental realization of an active elastic solid with active polar units connected by springs [Figs. 9(a) and 9(b)] was proposed by Baconnier *et al.* (2022). They focused on mechanically stable ordered lattices, where each node has a well-defined equilibrium reference position but is displaced by the active agent. In contrast, each agent is free to rotate and to self-align with its displacement. This nonlinear feedback between deformation and polarization is characterized by two length scales: the typical elastic deformation caused by active forces  $l_e$  and the self-alignment length  $l_a$ .

For small elastoactive coupling  $\Pi = l_e/l_a$ , the dynamics is disordered: displacements are small, and so is reorientation by motion; therefore, angular noise dominates the polarity

dynamics and randomizes the orientations. In contrast, for large enough  $\Pi$ , collective actuation emerges. When the system is pinned at the edges, the collective actuation takes the form of synchronized chiral oscillations of the lattice nodes around their reference configuration [see Fig. 9(c)], here also spontaneously breaking the chiral symmetry present at the level of each agent. When the pinning takes place on a central node, both forbidding translation and free rotation, a global alternating rotation of the entire structure, analogous to the oscillations of a torsion pendulum, emerges; see Fig. 9(d). A closer examination of the dynamics reveals that in both cases only a few normal modes are actuated, and, crucially, they are not necessarily the lowest energy ones.

The dimensionless Newton equations describing this model experimental system correspond to Eq. (4) in the case where  $w = v$ , with the external force  $F_{\text{ext}}$  given by the sum of the forces exerted by the elastic springs on each node. Using the spring rest length  $l_0$  and  $t_0 = \gamma/k$  as length and time units, the dimensionless equations read

$$\tau_v \ddot{\mathbf{r}}_i = \tilde{F}_a \hat{\mathbf{n}}_i - \dot{\mathbf{r}}_i + \sum_{j \in \partial i} (|\mathbf{r}_i - \mathbf{r}_j| - 1) \hat{\mathbf{e}}_{ij}, \quad (20a)$$

$$\tilde{\tau}_n \dot{\hat{\mathbf{n}}}_i = (\hat{\mathbf{n}}_i \times \dot{\mathbf{r}}_i) \times \hat{\mathbf{n}}_i + \sqrt{2\tilde{D}\xi} \hat{\mathbf{n}}_i^\perp, \quad (20b)$$

where  $\tau_v = mk/\gamma^2$ ,  $\tilde{\tau}_n = 1/\beta l_0 = l_a/l_0$ , and  $\tilde{F}_a = F_a/k l_0 = l_e/l_0$ .

The collective activation dynamics is described in the overdamped limit and in the context of the harmonic approximation, for which Eqs. (20a) and (20b) simplify to

$$\dot{\mathbf{u}}_i = \Pi \hat{\mathbf{n}}_i + \sum_j \mathbb{M}_{ij} \mathbf{u}_j, \quad (21a)$$

$$\dot{\hat{\mathbf{n}}}_i = (\hat{\mathbf{n}}_i \times \dot{\mathbf{u}}_i) \times \hat{\mathbf{n}}_i + \sqrt{2D\xi} \hat{\mathbf{n}}_i^\perp, \quad (21b)$$

where  $\mathbf{u}_i = \mathbf{r}_i - \mathbf{r}_i^0$  is the displacement of the agent  $i$  away from its reference configuration, now expressed in units of  $l_a$ ,  $\mathbb{M}$  is the dynamical matrix of the underlying elastic structure and  $\Pi = \beta \tilde{F}_a = l_e/l_a$ . This simplification allowed Baconnier *et al.* (2022) to show that the mode selection results from the nonlinear elastoactive feedback, resulting from self-alignment, which connects the linear destabilization of the fixed points to the spatial extension and the orthogonality of the polarization of the selected modes.

Performing simulations for large system sizes, the transition from the disordered phase to the synchronized chiral oscillations is observed to be discontinuous, with a transitional regime of spatial coexistence between the two phases that is controlled by the pinning condition. Baconnier *et al.* proposed a coarse-grained version of the dynamical equation,

$$\partial_t \mathbf{u} = \Pi \mathbf{m} + \mathbf{F}_e, \quad (22a)$$

$$\partial_t \mathbf{m} = (\mathbf{m} \times \partial_t \mathbf{u}) \times \mathbf{m} + \frac{1 - \mathbf{m}^2}{2} \partial_t \mathbf{u} - D_r \mathbf{m}, \quad (22b)$$

where  $\mathbf{u}(\mathbf{r}, t)$  and  $\mathbf{m}(\mathbf{r}, t)$  are the local averages of the microscopic displacements  $\mathbf{u}_i$  and polarizations  $\hat{\mathbf{n}}_i$ , respectively.

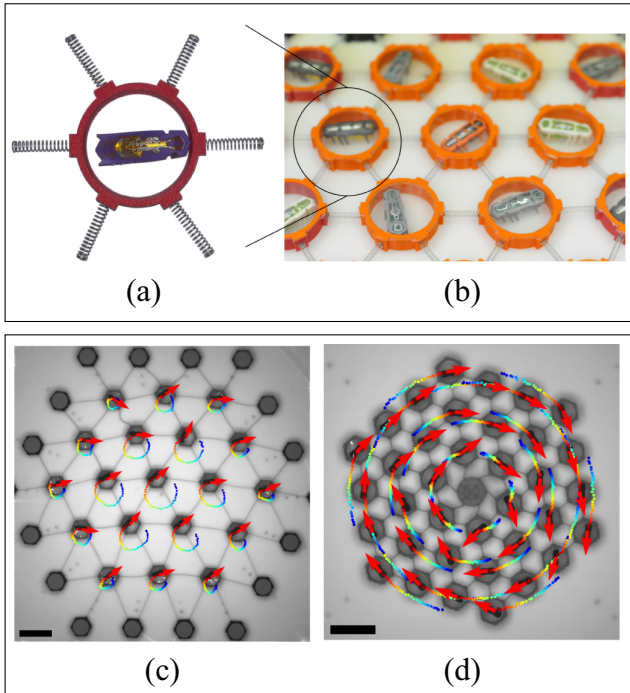


FIG. 9. Collective actuation in model active elastic structures. (a) Active elastic building blocks composed of a Hexbug inside a rigid annulus (b) are assembled with springs to form an active elastic network. Adapted from Baconnier *et al.*, 2022, and Hernández-López *et al.*, 2024. (c) Synchronized translational oscillations around the mechanical equilibrium configuration of a triangular lattice pinned at its edges. Adapted from Baconnier *et al.*, 2022. (d) Global alternating rotations of a triangular lattice with embedded central pinning. The trajectories are color coded from blue to red by increasing time. The red arrows indicate the polarities  $\hat{\mathbf{n}}_i$  at a given time. Scale bars, 10 cm. Adapted from Hernández-López *et al.*, 2024.

The elastic force  $\mathbf{F}_e[\mathbf{u}]$  is given by the choice of a constitutive relation, and the relaxation term  $-D_r \mathbf{m}$  results from the noise. Note that the second term in Eq. (22b), which arises from the coarse-graining procedure, allows the displacement's rate to polarize the elastic medium. Solving these equations for homogeneous solutions (Baconnier *et al.*, 2022; Baconnier, Démery, and Dauchot, 2024), one finds two coexisting solutions that are disconnected in phase space: a static disordered one with zero magnetization and a strongly magnetized oscillating chiral one. Future research directions include the possibility of designing the actuation dynamics by selectively choosing the nodes that are active (Lazzari, Dauchot, and Brito, 2024).

## B. Active jamming

In light of the aforementioned results, one would expect a similar collective actuation to take place in jammed packings of soft active particles with self-alignment. As the system is jammed, its structure is essentially frozen, and therefore the dynamics should not differ significantly from those reported previously in the review. Active jamming was proposed as a first step to describe the *in vitro* experiments on confluent

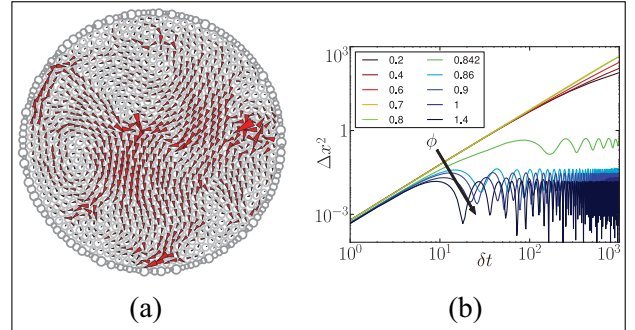


FIG. 10. Collective actuation of a jammed packing of soft particles. (a) Snapshot of the dynamics obtained from the simulation of a jammed packing of self-aligning soft polar disks described by Eq. (23). The outer glued boundary is shown in dark gray, while the red arrows represent the instantaneous velocity field, with  $v = v_0$  corresponding to an arrow of length 1 in units of the particle diameter. (b) Mean-square displacement as a function of time lag for different packing fractions  $\phi$  at fixed  $v_0$  showing a transition from diffusion at low  $\phi$  to polar alignment for  $\phi < 0.8$  to an oscillating jammed state around  $\phi = 0.842$ . Adapted from Henkes, Fily, and Marchetti, 2011.

monolayers of migratory epithelial and endothelial cells (Henkes, Fily, and Marchetti, 2011). The model considers  $N$  polar soft disks of radius  $a_i$ , position  $\mathbf{r}_i$ , and orientation  $\hat{\mathbf{n}}_i$  of which evolve with the overdamped equations of motion,

$$\dot{\mathbf{r}}_i = v_0 \hat{\mathbf{n}}_i + \alpha \sum_{j=1}^{z_i} \vec{F}_{ij}, \quad (23a)$$

$$\dot{\theta}_i = \frac{1}{\tau_a} (\psi_i - \theta_i) + \eta_i, \quad (23b)$$

The soft repulsive interaction force between the  $i$ th and  $j$ th disks is defined by  $\mathbf{F}_{ij} = -k(a_i + a_j - r_{ij})\hat{\mathbf{e}}_{ij}$  if  $r_{ij} < a_i + a_j$  and defined by  $\mathbf{F}_{ij} = 0$  otherwise. The self-alignment term is identical to the one introduced by Szabó *et al.* (2006) and corresponds to the linearization of the self-alignment in the case where  $\mathbf{w} = \hat{\mathbf{v}}$ . The angular noise  $\eta_i$  is considered as Gaussian with zero mean and variance  $\langle \eta_i(t)\eta_j(t') \rangle = \sigma^2 \delta_{ij} \delta(t - t')$ .

This model was studied in a circular confined geometry with polydisperse soft particles to avoid unrealistic crystallization effects in the dense phase. A self-actuating or oscillating phase emerges for small noise values at densities above the jamming transition  $\phi_J \approx 0.842$  and at small self-propulsion velocities; see Figs. 10(a) and 10(b). At larger velocities a uniformly rotating state emerges, followed by a reemergence of the circular swarm state, as analyzed by Szabó *et al.* (2006), at moderate densities. The self-actuating state was then analyzed using a normal mode formalism by projecting the motion onto the normal modes of the packing computed at the passive, minimized potential energy state nearest to the average particle positions. The motion shows regular oscillations with a frequency that corresponds directly to the lowest available normal mode in the confined system, and with significant coupling to only five to ten of the lowest modes. This was confirmed using a linear response calculation

that maps the motion to a damped oscillator in the normal modes, with a frequency proportional to the mode stiffness  $K_\nu$  and damping that vanishes for the lowest excited mode.

### C. Active Voronoi models in confinement

The self-propelled Voronoi model introduced in Sec. IV.C and Eq. (18) is a more realistic model of collective cell mechanics than the simple particles of (Szabó *et al.*, 2006; Henkes, Fily, and Marchetti, 2011). A good model for tissue oscillations can thus be obtained by combining the SPV model with self-alignment and explicit tissue boundaries that allow for confinement. This was first implemented numerically by Barton *et al.* (2017). For SPV parameters that belong to a solid flocking phase in flat space, the model leads to steady-state oscillations in confinement with a phenomenology that is similar to the active jamming described by Henkes, Fily, and Marchetti (2011); see Fig. 11(a). A significant step further was achieved by Petrolli *et al.* (2019), who matched this model to an experiment by simulating long, thin cell sheets with fixed boundaries to match the long, thin experimental setup with cells confined to a quasi-1D channel by selective coating with fibronectin. As in experiments, the model kymograph displayed in Fig. 11(b) shows regular oscillatory phenomenology.

### D. Mechanical oscillations in bacterial colonies and tissues

The two collective actuation dynamics reported in the experimental model of active elastic structure, namely, the synchronized chiral oscillations and the global alternating rotation, were observed in a single system of millimeter-sized, quasi-2D, and disk-shaped *P. mirabilis* biofilms (Xu *et al.*, 2023); see Figs. 12(a) and 12(b). The biofilm, with the top surface exposed to air and the bottom surface in contact with agar that provides nutrients and substrate adhesion, is laterally confined by a rim of immobile bacteria. Under isotropic confinement, it exhibits the two topologically distinct global dynamics reported earlier and a transition between the two regimes when tuning the activity level. Similar control was achieved in the case of the toy model elastic structure

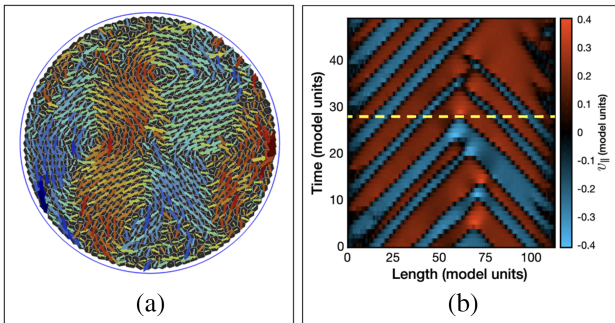


FIG. 11. Collective actuation in a self-propelled Voronoi model in confinement. (a) Simulated tissue in circular confinement in the solid flocking phase showing the velocity field in steady-state oscillation ( $p_0 = 3.385$  and  $J = 1$ ). Adapted from Barton *et al.*, 2017. (b) Kymograph (spacetime plot) of the velocity along a quasi-one-dimensional channel of simulated cells. Adapted from Petrolli *et al.*, 2019.

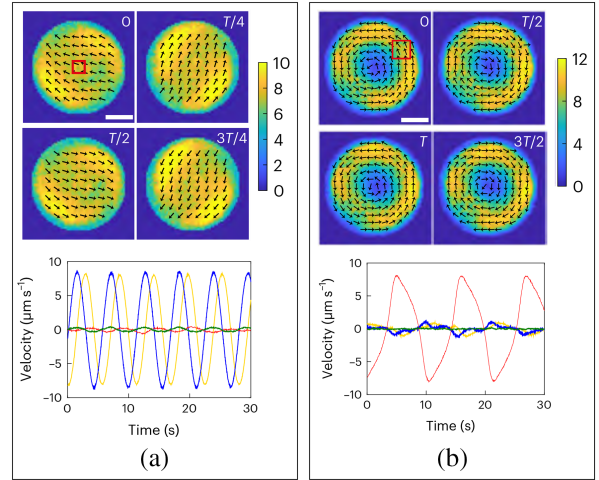


FIG. 12. Collective oscillations in bacterial biofilms. (a) Oscillatory translation along circular orbits and (b) oscillatory global rotation. Top panels: time sequences of the collective velocity field. Arrows represent the velocity directions, and the color map indicates the velocity magnitude in  $\mu\text{m/s}$ . Scale bar, 500  $\mu\text{m}$ . Bottom panels: temporal dynamics of the spatially averaged collective velocity decomposed into Cartesian (yellow and blue traces) and polar-coordinate (red: azimuthal, green: radial) components. Adapted from Xu *et al.*, 2023).

(Baconnier, 2023). The biofilm also exhibits self-sustained elastic waves with a power-law scaling of the wave speed with activity (Xu *et al.*, 2023). Xu *et al.* reproduced their finding in a model of overdamped self-aligning self-propelled particles connected by Hookean springs in a 2D triangular lattice, which is close to the one introduced by Baconnier *et al.* (2022) to describe the model experimental active elastic structures. The global alternating rotation dynamics was also observed in a dense active suspension of *Escherichia coli* confined in a viscoelastic fluid, the rheology of which is controlled by the addition of purified genomic DNA (Liu *et al.*, 2021). This behavior is explained by the interplay between active forcing and viscoelastic stress relaxation without explicit reference to a self-alignment mechanism. However, as Liu *et al.* used a coarse-grained model, this explanation does not preclude the existence of self-alignment at the microscopic scale.

Epithelial cell sheets are often subjected to large-scale deformation during tissue formation and the active mechanical environment in which they operate is known to promote collective oscillations. For instance, epithelial monolayers of Madin-Darby canine kidney (MDCK) cells in circular confinement exhibit swirling flows, which rely on the interplay of confinement and local alignment (Doxzen *et al.*, 2013). This swirling flow can be supplemented by a subdominant radial oscillation (Deforet *et al.*, 2014; Notbohm *et al.*, 2016). Analyzing the collective motion of epithelial cells confined to a quasi-one-dimensional channel in the light of numerical simulations, based on a self-propelled Voronoi model (see Sec. V.C), recent works (Petrolli *et al.*, 2019) showed that tuning the length of the confining channel drives a phase transition between a state of global oscillations and a multi-nodal wave state; see Fig. 13(a). This transition is a consequence of the interplay between local cell active dynamics and

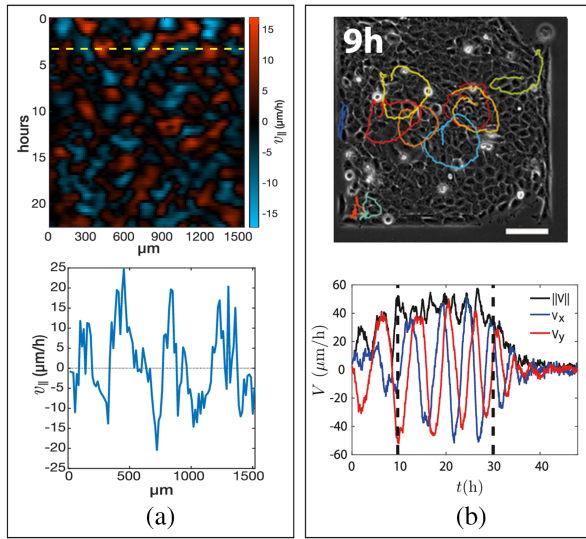


FIG. 13. Collective oscillations in tissues. (a) The velocity field of MDCK cells seeded onto a polyacrylamide gel patterned with fibronectin stripes are measured by PIV. Top image: kymograph representing the average horizontal velocity  $v_{\parallel}(x; t)$  demonstrates the presence of spatial and horizontal oscillations. Bottom panel: example of the velocity profile along the dashed line. Adapted from [Petrolli \*et al.\*, 2019](#). (b) Dynamics of a confluent HaCaT monolayer in square confinement. Top image: snapshots of the cell monolayer superimposed with representative trajectories of single cells performing translational oscillations along circular orbits. Scale bar, 100 mm. Bottom panel: time evolution of the two projected components,  $V_x = \langle v_x \rangle_{ROI}$  and  $V_y = \langle v_y \rangle_{ROI}$ , and norm of the velocity  $\|V\| = (V_x^2 + V_y^2)^{1/2}$  computed on a cropped area in the center of the square of the top image. Adapted from [Peyret \*et al.\*, 2019](#).

global confinement. The effect is demonstrated to rely on self-alignment. Also noteworthy are the dynamics reported in the case of human keratinocytes (HaCaT) and enterocytes (Caco2), where all cells perform a synchronized chiral oscillation ([Peyret \*et al.\*, 2019](#)); see Fig. 13(b). Using molecular perturbations, Peyret *et al.* demonstrated that force transmission at cell-cell junctions and its coupling to cell polarity are pivotal for the generation of these collective dynamics. This system was then modeled using self-alignment dynamics with a phase-field model of the tissue, where each phase corresponds to an individual deformable cell.

## VI. DISCUSSION AND PERSPECTIVES

### A. A unified framework?

The models discussed in this review (see Table I) distinguish themselves by the role of elasticity and by the type of boundary condition. They can also include translational and/or rotational inertia or no inertia. Most importantly, they differ by the way self-alignment was phenomenologically introduced. In this section we discuss how far one can formulate a unified framework for these different classes of self-aligning polar agents.

We start by addressing the role of inertia. Active Brownian particles were first introduced as fully overdamped polar

active particles without alignment. The model was later upgraded in a series of papers ([Scholz \*et al.\*, 2018](#); [Löwen, 2020](#)) by including inertia in both the translational and the orientational motion. Analytical results were obtained for the orientational and translational correlation functions of the single-particle dynamics, displaying good agreement with experiments using vibrated granular systems. More exact analytical predictions for higher-order statistics were also obtained by devising an inertial active Ornstein-Uhlenbeck particle, which further simplifies the active Brownian dynamics by enforcing Gaussian fluctuations ([Sprenger \*et al.\*, 2023](#)). More specifically, it was shown that rotational inertia is fundamentally relevant to reproduce the temporal delay between the active force and particle velocity observed for a single active granular particle.

Obtaining similar results for inertial self-aligning particles would be of great interest. Thus far, the only work considering both angular and translational inertia for self-aligning particles is limited to deterministic dynamics ([Fersula, Bredeche, and Dauchot, 2024](#)). Furthermore, the results in the work of Fersula, Bredeche, and Dauchot suggest that accounting for fluctuations will be a difficult task. Indeed, they demonstrated that the coupling of self-alignment with angular inertia produces unexpected nontrivial dynamics already at the deterministic level, including the coexistence of different solutions and unexpected oscillations that take place when one considers interaction with a wall.

Regarding the simpler case of translational inertia with overdamped angular dynamics, it was considered both when studying the dynamics of a single self-aligning polar agent in a harmonic potential (Sec. III.B) and when modeling the collective dynamics of the vibrated disk experiment (Sec. IV.A). In the first case, it was shown analytically that translational inertia does not alter the fixed points or the orbiting solutions. It merely modifies the stability region of the latter and, when large enough, it leads to a coexistence in phase space of the stable climbing solution and the stable orbiting one. However, existing experimental systems fall far short of reaching this level of translational inertia. Regarding the collective dynamics of vibrated disks, including translational inertia, was required to obtain a quantitative mapping between the numerical simulations and the experiments ([Weber \*et al.\*, 2013](#)). Translational inertia also plays a role in the precise shape of the phase diagram for the transition to collective motion computed by [Lam, Schindler, and Dauchot \(2015a, 2015b\)](#) and shown in Fig. 4(a), but it does not qualitatively change the picture of the transition to collective motion for self-aligning polar agents. Altogether, these analyses suggest that translational inertia can be safely neglected in most contexts considered to date.

We now discuss the way self-alignment was introduced on a phenomenological basis. The model variants regarding the coupling between the translational and rotational dynamics can be distinguished according to the following conditions:

- Whether the alignment strength is proportional to the amplitude of the velocity ( $w = \mathbf{v} = \dot{\mathbf{r}}$ ) or not proportional to the amplitude of the velocity ( $w = \hat{\mathbf{v}}$ ).
- Whether the aligning torque is linearized (L) or not linearized (NL).

According to the mechanical model described in Sec. II and detailed in Appendix A, the self-alignment torque should read  $\mathbf{T}_{sa} = \gamma(\mathbf{r}_m - \mathbf{r}_f) \times \dot{\mathbf{r}}_m$ , corresponding to the case  $\mathbf{w} = \mathbf{v} = \dot{\mathbf{r}}$ . A key requirement for inducing self-alignment in the model is thus that the center of mass  $\mathbf{r}_m$  differs from the center of friction  $\mathbf{r}_f$ . The aligning or antialigning dynamics arise from the parallel or antiparallel character of the self-propulsion direction  $\hat{\mathbf{n}}$  with respect to the vector  $\mathbf{r}_m - \mathbf{r}_f$ . This is indeed the case in the experiment described in Sec. III.A, where a Hexbug is driven along the side of a square, and for the self-aligning polar agents illustrated in Fig. 2(c), where two different exoskeleton designs mounted on simple walkers change the sign of the self-aligning torque.

Despite the previous discussion, one cannot exclude the possibility that, in a more complex form of self-propelled agent (for example, with a deformable body), the self-alignment strength could have a different dependence on the amplitude of the velocity  $\mathbf{v}$ . It is thus of interest to clarify what qualitative difference the choice of  $\mathbf{w} = \mathbf{v}$  or  $\mathbf{w} = \hat{\mathbf{v}}$  can have on the dynamics. For instance, in the Supplemental Material of Dauchot and Démery (2019), it was shown that making the choice  $\mathbf{w} = \hat{\mathbf{v}}$  suppresses the frozen, climbing state of a Hexbug in a harmonic potential and that the orbiting state is observed for any positive value of the coupling parameter.

To assess the generality of these results, we introduce a more general model for the angular dynamics:

$$\dot{\theta} = \beta |\mathbf{v}|^\nu f[(\hat{\mathbf{n}} \times \hat{\mathbf{v}}) \cdot \hat{z}]. \quad (24)$$

The choice  $\nu = 1$  thus corresponds to  $\mathbf{w} = \mathbf{v}$ , while  $\nu = 0$  corresponds to  $\mathbf{w} = \hat{\mathbf{v}}$ . The function  $f[x]$  is given by  $f[x] = x$

when the aligning torque is NL and given by  $f[x] = \sin^{-1}(x)$  when it is L. In general, it should be a nonsingular odd function with a domain given by  $[-1, 1]$ . At the single-particle level, analyzing the stationary states and the stability of the frozen state in a harmonic potential (Appendix B), we find that for  $\nu < 1$  chiral states are observed for all the values of the alignment parameter  $\beta$ , while for  $\nu = 1$  they are observed only beyond a threshold  $\beta_c$ . For  $\nu > 1$  multiple chiral states may exist. The results are largely independent of the particular choice of  $f[x]$ .

At the collective level, synchronous oscillations were reported whether  $\mathbf{w} = \mathbf{v}$  or  $\mathbf{w} = \hat{\mathbf{v}}$ , but for different systems. The case  $\mathbf{w} = \mathbf{v}$  was discussed in the context of elastic structures, while that with  $\mathbf{w} = \hat{\mathbf{v}}$  was considered for dense assemblies of soft particles. To clarify the situation, we have run simulations of Eqs. (5), with  $\mathbf{w} = \mathbf{v}$  and  $\mathbf{w} = \hat{\mathbf{v}}$ , in jammed assemblies of particles and an elastic network; see Fig. 14. Regardless of the system of interest, when  $\mathbf{w} = \mathbf{v}$ , there is a regime at small self-alignment where collective actuation does not take place, and the transition first reported in the case of elastic structures is also observed in the case of jammed assemblies of soft particles, while in the case of  $\mathbf{w} = \hat{\mathbf{v}}$  collective actuation takes place for arbitrary small values of the self-alignment. Hence, the collective behavior essentially inherits here the property analyzed at the single-particle level.

## B. Large-scale hydrodynamics theory

Large-scale hydrodynamics formulations of dry active matter were introduced as early as 1995 to describe the flocking phase of polar liquids (Toner and Tu, 1995). Soon thereafter, the case of active nematic liquids on a substrate was also considered (Ramaswamy, Simha, and Toner, 2003).

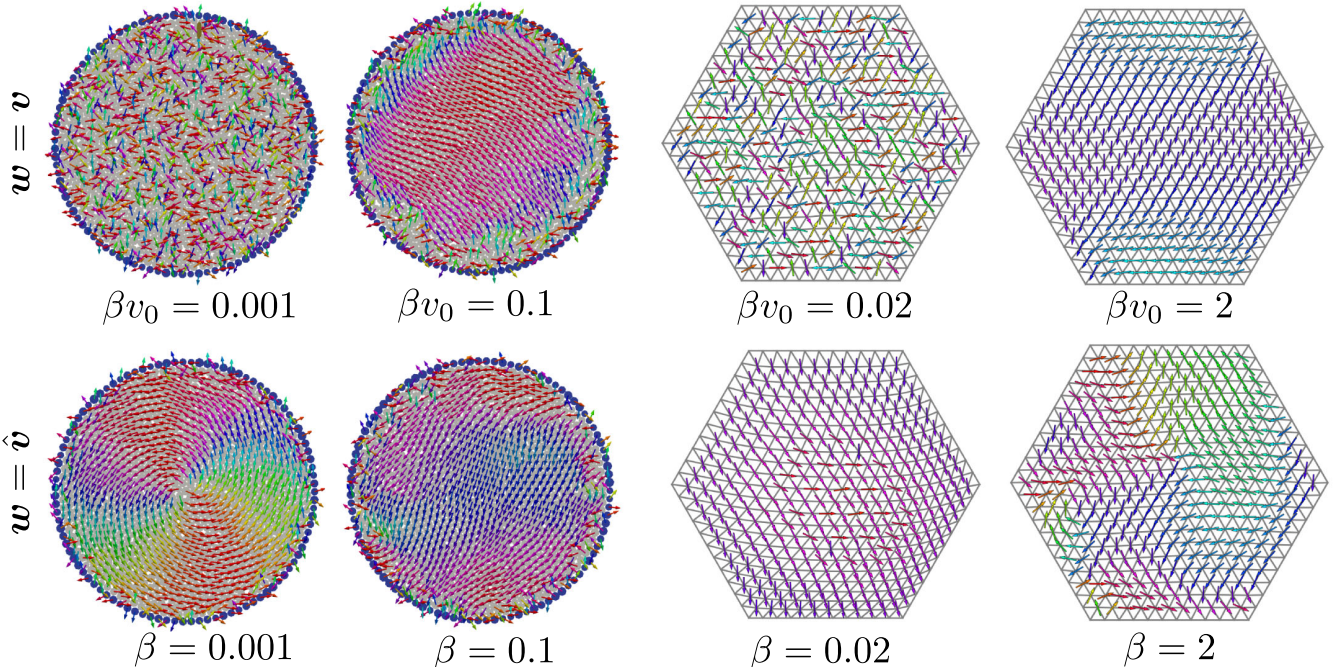


FIG. 14. Collective actuation in particle systems (left images) and elastic network (right images) for  $\mathbf{w} = \mathbf{v}$  and  $\mathbf{w} = \hat{\mathbf{v}}$ , respectively. Images were obtained from simulating Eq. (5) with the appropriate interactions (harmonic repulsion or harmonic springs) and in the limit of small angular noise.

In both cases the phases that were considered are liquids of particles taking their momentum from the ground. The theory of active gels, on the contrary, was introduced to describe the mechanical behavior of cells, assuming momentum conservation (Kruse *et al.*, 2004, 2005). In addition, it accounts for a short-time elastic regime that is captured by introducing a Maxwell timescale in the constitutive relation. Such hydrodynamic theories were obtained from a perturbative expansion around a specific ordered state (Toner and Tu, 1995; Ramaswamy, Simha, and Toner, 2003), the existence and stability of which is not guaranteed or by introducing constitutive equations between the fluxes and the forces identified from the entropy production rate close to equilibrium (Kruse *et al.*, 2004), at the cost of leaving aside systems that are far from equilibrium. Alternatively, one can write down a microscopic theory and coarse grain it to obtain the hydrodynamic equations for the large-scale fields (Marchetti *et al.*, 2013). There are several ways to implement such an explicit coarse-graining procedure, depending on their starting points. One can start with a Boltzmann equation describing the dynamics of the one-particle probability density (Boltzmann, 1872). This approach has been followed for polar particles with polar (Bertin, Droz, and Grégoire, 2009; Peshkov *et al.*, 2014) and nematic alignment (Bertin *et al.*, 2013) for Janus particles avoiding dense regions (Zhang *et al.*, 2021) and for colloidal rollers interacting hydrodynamically (Bricard *et al.*, 2013). One could also start one step ahead, with the Smoluchowski equation for the  $N$ -body probability density (te Vrugt, Löwen, and Wittkowski, 2020), as exemplified in an analysis of the phase separation of self-propelled repulsive disks (Bialké, Löwen, and Speck, 2013), or with the Dean equation (Dean, 1996), a Langevin equation for the microscopic density field, as illustrated by the derivation of the active model B+ (Tjhung, Nardini, and Cates, 2018) and the discussion of the motility-induced phase separation in the presence of velocity alignment (Barré *et al.*, 2015). In all cases this difficult task is paved with approximations that are not always well controlled. Nevertheless, active hydrodynamic theories have the advantage of being generic in the sense that they are able to describe different systems, provided that these share the same conservation laws and symmetries.

The polar systems discussed in the context of this review take their momentum from the ground and therefore belong to the so-called class of dry polar active matter, for which there is no conservation of momentum. Their liquid phase is therefore described by Toner-Tu-like equations (Toner and Tu, 1995; Toner, Tu, and Ramaswamy, 2005), and the Landau terms of these equations were explicitly derived for self-aligning disks, thus demonstrating that self-alignment effectively leads to collective motion (Lam, Schindler, and Dauchot, 2015a, 2015b), as discussed in Sec. IV.A.

The case of active solids was considered only more recently. A first approach is to couple phase-field crystals with the Toner-Tu equations to describe solid polar flocks (Menzel and Löwen, 2013; Alaimo, Praetorius, and Voigt, 2016; Ophaus, Gurevich, and Thiele, 2018). This, however, ignores a symmetry-mandated coupling between orientation and strain due to rotation invariance. In passive orientationally ordered solids, such a coupling leads to the vanishing of the zero-frequency shear modulus (Dalheimer, Discher, and

Lubensky, 2007). The role of activity includes the possibility of stable uniaxial active solids when momentum is not conserved, and the instability of the uniaxially ordered phase in momentum-conserved systems for large active forcing (Maitra and Ramaswamy, 2019). In all cases such theories of active solids have thus far considered oriented active solids, that is, active solids with polar or nematic order. In the context of this review, they predict the stability at large scale of collective motion in the active sheet.

A complementary approach is to consider scalar active solids, where activity stems from nonconservative interaction forces (Scheibner *et al.*, 2020). Considering the case where momentum is conserved, the forces derive from a stress tensor, which in the limit of small strain is linearly related to the strain tensor by the static elastic modulus tensor, as is the case for the usual passive elastic materials. However, static elastic moduli altogether absent in passive elasticity can arise from the active, nonconservative microscopic interactions. These active moduli enter the antisymmetric part of the static elastic modulus tensor—hence the name “odd elasticity”—and quantify the amount of work extracted along quasistatic strain cycles. The application of these ideas to the systems described here is not straightforward, because the absence of momentum conservation gives rise to forces that do not derive from a stress tensor. However, the self-alignment is likely to contribute to the active part of the stress tensor, including the odd part of it.

Altogether, the large-scale physics of active systems composed of self-aligning active agents remains largely unexplored. In the liquid polar state, the computation of the Landau terms of the Toner-Tu equation demonstrates that the mean-field transition to collective motion can be first order, in sharp contrast to the case of the Vicsek model. The consequences of it beyond the mean field remain unknown. The solid polar state is stable at large scale (Maitra and Ramaswamy, 2019); however, the role of structural defects remains unexplored. The mechanical response of such active solids, with the possibility of odd elasticity, also remains unexplored. Finally, the fate of the transition to collective actuation at large scale is unknown. One possible avenue for making progress in this last direction is the possible connection with nonreciprocal phase transitions.

### C. Connection with nonreciprocal phase transitions

It was recently shown that systems composed of microscopic degrees of freedom experiencing nonsymmetrical interactions, together with nonconservative dynamics, are prone to develop chiral phases via a specific kind of phase transition called nonreciprocal (Fruchart *et al.*, 2021), which are controlled by the presence of exceptional points. Self-alignment can be seen as a nonreciprocal internal coupling between the displacement and the orientation within each active particle: the polarity aligns with the displacement rate, while the displacement evolves following the sum of active and elastic forces. At the level of a single active particle in a harmonic potential, in the case  $w = v$ , the polarity and displacement vectors explicitly experience nonsymmetrical interactions. Eliminating adiabatically the dynamics of the amplitude of the displacement, one finds that the phase of the

displacement vector is chasing that of the polarity (Henkes, Fily, and Marchetti, 2011; Baconnier, 2023). It is also found not only that the transition takes place through an exceptional point but also that the entire orbiting, or chiral, phase stands on a line of exceptional points in the parameter space. At the level of the coarse-grained equations [Eqs. (22)], when linearizing them around the disordered phase and mapping them to the most general equations, one can write for rotationally symmetric vectorial order parameters, one finds that the macroscopic displacement and polarity fields also couple nonsymmetrically (Baconnier *et al.*, 2022).

Nonreciprocal phase transitions could therefore be a good paradigm to discuss the transition to collective actuation. A more precise analysis, however, remains to be done. In particular, the transition considered here takes place from the disordered to the chiral phase, while that discussed in the context of nonreciprocal phase transitions arises from the polar or antipolar phase.

#### D. Further perspectives

We conclude this review by offering a few perspectives that we believe to be promising research avenues. At the conceptual level, the increasing importance of self-alignment as a generic mechanism for collective actuation in active solids is likely to raise many theoretical developments. As mentioned, a general continuous description of dry active solids, not to mention the mechanical properties of such solids, from linear elasticity to plasticity and failure, is still missing. The stability of collective actuation in the thermodynamic limit remains to be investigated. Since collective actuation results from the coupling of a spinlike degree of freedom to the vibration of the elastic structure, it could be interesting to probe the response to an external polarizing field: controlling the orientation of the agents with an external field could be a practical way of controlling the actuation locally.

In a different vein, it was recently shown that bulk or boundary disorder are relevant to active systems because of the presence of long-range density and current modulations (Morin *et al.*, 2017; Besse, Chaté, and Solon, 2022; Benvennen *et al.*, 2023; Granek *et al.*, 2024). This is also true for any amount of anisotropy, which drastically alters the phenomenology of flocking from that of the rotationally invariant case (Solon *et al.*, 2022). The precise properties of collective actuation in the presence of disorder are a central issue for any practical application. Different types of disorder must be considered. The elastic structure can, for instance, include several types of defects or can instead correspond to an inherently disordered jammed or glassy packing. One may also want to consider disorder in the self-aligning strength or the effect of a random external field. Given that elastic modes will couple differently in the presence of disorder, one can expect interesting new behaviors such as localization of the actuation.

A last general question concerns the sign of the self-aligning torque. It was realized only recently that negative self-alignment can lead to interesting dynamics (Ben Zion *et al.*, 2023), and there has not yet been a systematic study of the collective dynamics of a large assembly of self-antialigning particles. When two such particles collide, they point toward each other,

leading to an effective adhesion that can be much stronger than in the case of scalar active matter. It is thus likely that such particles will experience motility-induced phase separation at low packing fraction, even for moderate persistence time. In addition, the coupling of antialignment with elastic interactions to date remains completely unexplored.

In the context of swarm robotics, it was shown that the sign of self-alignment can be influential in the way that a swarm of robots solves a simple phototactic task, with strong steric frustration (Ben Zion *et al.*, 2023), and can make it an essential ingredient of self-organization and function. For example, in biological organisms like *Trichoplax adhaerens*, self-alignment is thought to play a role in setting large-scale coordination and complex forms of locomotion (Davidescu *et al.*, 2023). The complex dynamics and the different modes of collective motion of elastic structures doped with self-aligning active agents are thus an interesting direction to create autonomous robots exploring their environment and interacting with it.

In dense biological systems like cell monolayers and bacterial biofilms, self-alignment is not the only contribution to the repolarization of the microscopic agents. For monolayers explicit active coupling between contractile junctions with nematic symmetry and mechanochemical feedback need to be considered (Rozman, Yeomans, and Sknepnek, 2023; Sknepnek *et al.*, 2023), and in bacterial biofilms explicit nematic shape alignment has to be taken into account. This begs the question of how informative the empirically observed emerging collective dynamics on the properties of the microscopic constituents is. Can one state that self-alignment is present or dominant, even effectively, if collective actuation is observed? Thus, constructing an explicit test for self-alignment becomes important. Since taking a single cell out of its environment irrevocably changes its phenotype, unlike for mechanical particles, this will need to take place at the collective level. A good avenue for this test will be to exploit the intimate relation of collective actuation to elastic normal modes and vary the system size and boundary conditions to make predictions.

## VII. CONCLUSION

In this review we have reported the numerous occasions where self-alignment manifests itself in the field of polar active matter. Although this generic, mechanically rooted coupling between the polarity and the velocity of a self-propelled particle was introduced as early as 1996, it remained overlooked for a long time, mostly because it was thought that its specificity could be integrated out into some form of mutual alignment at the effective level. This vision, which is partly correct when the emergence of collective motion is considered, misses the potentiality offered by self-alignment when dense assemblies of self-propelled particles or elastic networks are considered. In that context, where the particle is essentially confined in a local harmonic potential, the natural tendency of a self-aligning particle to perform orbiting motion, as a result of a spontaneously broken chiral symmetry, leads to unanticipated forms of collective dynamics.

These new dynamics are prominent in the realm of biological systems such as bacterial rafts and tissues and are likely to play a crucial role in large-scale synchronization

phenomena. Indeed, given that some cells have been shown to follow self-alignment rules, evolution has likely exploited this mechanism to achieve self-organization in multiple contexts. It could be relevant, for example, in the collective migration of tumor cells or in the formation of structures during organism development. The medical applications that could stem from a better understanding of self-alignment could thus be wide-ranging.

In the context of metamaterials, self-alignment can be implemented in multiple ways by integrating passive mechanics with actuators that, in the future, could be mass produced and miniaturized. This will allow the manufacturing of materials with unique rheological properties, such as continuing to deform as prompted after all external stresses have stopped. These materials could also potentially control their modes of self-organized collective actuation, allowing the design of specific actuation patterns that result in new autonomous functions. There are therefore also great potential applications of self-alignment to material sciences.

Finally, in the context of swarm robotics, self-alignment allows for simpler computation rules among agents, which need to evaluate only their neighbors' positions, not their velocities. In fact, in some contexts self-alignment can even be introduced through a mechanical coupling between robots, with its dynamics becoming part of the embodied computations in a robot swarm. This simplicity of implementation of self-alignment could be useful in systems where the sensing and control capabilities are limited in order to reduce the size, complexity, or cost of each agent. The robustness of the collective dynamics emerging from self-alignment could also facilitate the development of robot swarms that perform reliably in noisy environments and with limited sensing. We believe that self-alignment is opening promising new routes of research and hope that this review will serve as a useful guide to the diversity of models that have been independently introduced over the past 30 years.

## APPENDIX A: MECHANISMS FOR SELF-ALIGNMENT

### 1. Self-alignment of axisymmetric rigid walkers

We consider here an arbitrary body of volume  $\mathcal{W}$  held rigid by a distribution of pairwise internal forces  $f_{\text{int}}(\mathbf{r})$ , with a distribution of mass  $\tilde{m}(\mathbf{r})$ , a distribution of friction coefficient  $\tilde{\gamma}(\mathbf{r})$ , and a distribution of active and external forces  $f_{\text{act}}(\mathbf{r})$  and  $f_{\text{ext}}(\mathbf{r})$  acting upon it. The equations of motion applied to each point of this rigid solid read

$$\tilde{m}(\mathbf{r})\ddot{\mathbf{r}} = f_{\text{act}}(\mathbf{r}) - \tilde{\gamma}(\mathbf{r})\dot{\mathbf{r}} + f_{\text{ext}}(\mathbf{r}) + f_{\text{int}}(\mathbf{r}). \quad (\text{A1})$$

Introducing the center of mass  $\mathbf{r}_m = (1/m) \int_{\mathcal{W}} \tilde{m}(\mathbf{r}) \mathbf{r} d\mathbf{r}$ , with  $m = \int_{\mathcal{W}} \tilde{m}(\mathbf{r}) d\mathbf{r}$  the total mass, and the center of friction  $\mathbf{r}_f = (1/\gamma) \int_{\mathcal{W}} \tilde{\gamma}(\mathbf{r}) \mathbf{r} d\mathbf{r}$ , with  $\gamma = \int_{\mathcal{W}} \tilde{\gamma}(\mathbf{r}) d\mathbf{r}$  the effective friction coefficient, the equation of motion for the center of mass is obtained by integrating Eq. (A1) over  $\mathcal{W}$ ,

$$m\ddot{\mathbf{r}}_m = \mathbf{F}_a - \gamma\dot{\mathbf{r}}_f + \mathbf{F}_{\text{ext}}, \quad (\text{A2})$$

where  $\mathbf{F}_a = \int_{\mathcal{W}} f_{\text{act}}(\mathbf{r}) d\mathbf{r}$ ,  $\mathbf{F}_{\text{ext}} = \int_{\mathcal{W}} f_{\text{ext}}(\mathbf{r}) d\mathbf{r}$ , and the internal forces cancel out,  $\int_{\mathcal{W}} f_{\text{int}}(\mathbf{r}) d\mathbf{r} = 0$ .

Similarly, the equation for the angular degrees of freedom is obtained by integrating the local torques with respect to the center of mass,

$$\tilde{m}(\mathbf{r})\rho_m \times \ddot{\mathbf{r}} = \rho_m \times [f_{\text{act}}(\mathbf{r}) - \tilde{\gamma}(\mathbf{r})\dot{\mathbf{r}} + f_{\text{ext}}(\mathbf{r}) + f_{\text{int}}(\mathbf{r})], \quad (\text{A3})$$

where  $\rho_m = \mathbf{r} - \mathbf{r}_m$ . Recalling that for solid body rotation  $\dot{\mathbf{r}} = \dot{\mathbf{r}}_m + \boldsymbol{\Omega} \times \rho_m$  and that  $\ddot{\mathbf{r}} = \ddot{\mathbf{r}}_m + \dot{\boldsymbol{\Omega}} \times \rho_m + \boldsymbol{\Omega} \times (\boldsymbol{\Omega} \times \rho_m)$ , where  $\boldsymbol{\Omega}$  is the solid body rotation vector, and using  $\int_{\mathcal{W}} \tilde{m} \rho_m d\mathbf{r} = \mathbf{0}$  by definition, the integration of the left-hand side of Eq. (A3) leads to

$$\int_{\mathcal{W}} \tilde{m}(\mathbf{r})\rho_m \times \ddot{\mathbf{r}} = I_m \dot{\boldsymbol{\Omega}}, \quad (\text{A4})$$

with  $I_m = \int_{\mathcal{W}} \tilde{m}(\mathbf{r}) |\rho_m|^2 d\mathbf{r}$ . When the active and external torques  $\mathbf{T}_a = \int_{\mathcal{W}} \rho_m \times f_{\text{act}} d\mathbf{r}$  and  $\mathbf{T}_{\text{ext}} = \int_{\mathcal{W}} \rho_m \times f_{\text{ext}} d\mathbf{r}$  are introduced, the integration of the right-hand side of Eq. (A3) thus leads to

$$I_m \dot{\boldsymbol{\Omega}} = \mathbf{T}_a + \gamma(\mathbf{r}_m - \mathbf{r}_f) \times \dot{\mathbf{r}}_m - \gamma_r \boldsymbol{\Omega} + \mathbf{T}_{\text{ext}}, \quad (\text{A5})$$

with  $\gamma_r = \int_{\mathcal{W}} \tilde{\gamma}(\mathbf{r}) |\rho_m|^2 d\mathbf{r}$ .

Denoting  $\hat{\mathbf{n}}$  as the direction of the active force, we now specifically consider a polar active particle whose active forces and friction distributions are symmetric with respect to the axis aligned with  $\hat{\mathbf{n}}$  and going through the center of mass  $\mathbf{r}_m$ . In such a case,  $\mathbf{T}_a = \mathbf{0}$  and  $\mathbf{r}_m - \mathbf{r}_f$  and  $\hat{\mathbf{n}}$  are colinear, so we can define  $\zeta \hat{\mathbf{n}} = \gamma(\mathbf{r}_m - \mathbf{r}_f)$ . Equations (A2) and (A3) then read

$$m\ddot{\mathbf{r}}_m = \mathbf{F}_a \hat{\mathbf{n}} - \gamma \dot{\mathbf{r}}_f + \mathbf{F}_{\text{ext}}, \quad (\text{A6a})$$

$$I_m \dot{\boldsymbol{\Omega}} = \zeta \hat{\mathbf{n}} \times \dot{\mathbf{r}}_m - \gamma_r \boldsymbol{\Omega} + \mathbf{T}_{\text{ext}}, \quad (\text{A6b})$$

with

$$\dot{\mathbf{r}}_f = \dot{\mathbf{r}}_m + \boldsymbol{\Omega} \times (\mathbf{r}_f - \mathbf{r}_m), \quad (\text{A7})$$

where one recognizes Eq. (1) of the main text.

Four comments are of interest. First, one learns from this calculation that the sign of  $\zeta$  is governed by the relative position of the center of friction  $\mathbf{r}_f$  with respect to that of the center of mass  $\mathbf{r}_m$ . Second, the self-aligning torque with  $w = \dot{\mathbf{r}}_m / |\dot{\mathbf{r}}_m|$ , introduced in the literature on a phenomenological basis, has no clear mechanical justification. Third, and perhaps most importantly, previous works have assumed the equality of the velocities of the center of mass and the center of friction, which is not valid in the presence of self-alignment. Taking the equality into account properly amounts to an additional force term  $-\zeta \boldsymbol{\Omega} \times \hat{\mathbf{n}}$  acting perpendicularly to the active force when the particle body rotates.

However, we soon show that, for an overdamped dynamics, the assumption is reasonable as soon as  $b = |\mathbf{r}_f - \mathbf{r}_m|$  is small compared to the typical agent size  $R$ . Indeed, Eqs. (A6b) and (A7) read

$$\dot{\mathbf{r}}_f = \dot{\mathbf{r}}_m + \epsilon b \boldsymbol{\Omega} \times \hat{\mathbf{n}}, \quad (\text{A8a})$$

$$\gamma_r \dot{\theta} = \epsilon \gamma b (\hat{\mathbf{n}} \times \dot{\mathbf{r}}_m) \cdot \hat{\mathbf{z}}, \quad (\text{A8b})$$

where  $\epsilon = \pm 1$  and we have ignored the external torque, which plays no role in the argument. There are two length scales of interest: the alignment length  $l_a = \gamma_r / \gamma b$  and  $b$ . Using  $l_a$  as the unit length, we can rewrite Eqs. (A8a) and (A8b) as

$$\dot{\mathbf{r}}_f = \dot{\mathbf{r}}_m + \epsilon \frac{b}{l_a} \boldsymbol{\Omega} \times \hat{\mathbf{n}}, \quad (\text{A9a})$$

$$\dot{\theta} = \epsilon (\hat{\mathbf{n}} \times \dot{\mathbf{r}}_m) \cdot \hat{\mathbf{z}} + T^{\text{ext}}, \quad (\text{A9b})$$

where one sees that the validity of the assumption is controlled by the ratio  $b/l_a \simeq (b/R)^2$ , which is generally small.

Finally, in the overdamped limit, one notes that if the external force is not given by gravity, the center of mass becomes irrelevant for the dynamics. Therefore, it is convenient to consider the torque in Eq. (A6b) from the position at which the external torques vanish  $\mathbf{r}_\tau$ , if it exists, instead of the center of mass. This leads to a zero external torque in the self-alignment equation, where now all  $\mathbf{r}_m \rightarrow \mathbf{r}_\tau$ , meaning that  $\zeta$  is then given by  $\zeta \hat{\mathbf{n}} = \gamma(\mathbf{r}_\tau - \mathbf{r}_f)$  and  $\gamma_r = \int_{\mathcal{W}} \tilde{\gamma}(\mathbf{r}) |\mathbf{r}_\tau - \mathbf{r}|^2$ .

## 2. Self-alignment through nonaxisymmetric forces

Self-alignment can also emerge from other asymmetries. We consider a total of  $N$  off-centered disks, either rigidly connected with elastic springs (a rigid network) or elastically interacting with only their repulsive counterparts. The “off-centered” aspect suggests that the center of mass of these disks is not at their geometric centers. The center of mass of the  $i$ th particle  $\mathbf{r}_i^{\text{CM}}$  is defined as  $\mathbf{r}_i^{\text{CM}} = \mathbf{r}_i^{\text{CO}} \pm R \hat{\mathbf{n}}_i$ , where  $\mathbf{r}_i^{\text{CO}}$  is the position of the geometric center and  $R$  is the distance between the center of mass and the geometric center. The total interaction force acts on the  $i$ th disk  $\mathbf{f}_i = \sum_j \mathbf{f}_{ij}(\mathbf{r}_i^{\text{CM}}, \mathbf{r}_j^{\text{CM}})$ .

In overdamped dynamics the position of the  $i$ th off-centered object evolves as

$$\dot{\mathbf{r}}_i = v_0 \hat{\mathbf{n}}_i + \mathbb{M}_i \mathbf{f}_i, \quad (\text{A10})$$

where  $\mathbb{M}_i$  represents the mobility matrix, which is defined as  $\mathbb{M}_i = \mu_{||} \hat{\mathbf{n}}_i \hat{\mathbf{n}}_i + \mu_{\perp} (\mathbb{I} - \hat{\mathbf{n}}_i \hat{\mathbf{n}}_i)$ . We recover the evolution of the heading direction  $\hat{\mathbf{n}}_i$  by letting  $\beta = \bar{\beta} R$  as follows:

$$\dot{\hat{\mathbf{n}}}_i = \beta (\mathbf{f}_i \cdot \hat{\mathbf{n}}_i^\perp) \hat{\mathbf{n}}_i^\perp, \quad (\text{A11})$$

which is equivalent to  $\dot{\theta}_i = \beta (\hat{\mathbf{n}}_i \times \mathbf{f}_i) \cdot \hat{\mathbf{z}}$ . In this context, self-alignment emerges owing to the alignment of the heading direction  $\hat{\mathbf{n}}_i$  toward the total interacting force  $\mathbf{f}_i$ , unlike the alignment toward velocity  $v_i$  observed in the case of overdamped rigid walkers, as presented in Appendix A.1.

The self-alignment torques then emerge as explicit mechanical torques  $\tau_i = \bar{\beta} \sum_j \mathbf{r}_i^{\text{CM}} \times \mathbf{f}_{ij}(\mathbf{r}_i^{\text{CM}}, \mathbf{r}_j^{\text{CM}})$ , where  $\beta$  sets the strength of the self-alignment. This can be expressed as

$$\tau_i = \pm \bar{\beta} R \hat{\mathbf{n}}_i \times \sum_j \mathbf{f}_{ij}(\mathbf{r}_i^{\text{CM}}, \mathbf{r}_j^{\text{CM}}). \quad (\text{A12})$$

In this interpretation, when the center of mass is positioned toward the heading direction  $\hat{\mathbf{n}}_i$ , i.e.,  $\mathbf{r}_i^{\text{CM}} = \mathbf{r}_i^{\text{CO}} + R \hat{\mathbf{n}}_i$ , it leads to alignment  $\tau_i = \bar{\beta} R \mathbf{f}_i \cdot \hat{\mathbf{n}}_i^\perp$ . Conversely, when the center of mass is positioned opposite to the heading direction  $\hat{\mathbf{n}}_i$ , i.e.,  $\mathbf{r}_i^{\text{CM}} = \mathbf{r}_i^{\text{CO}} - R \hat{\mathbf{n}}_i$ , it results in antialignment,  $\tau_i = -\bar{\beta} R \mathbf{f}_i \cdot \hat{\mathbf{n}}_i^\perp$ . In this scenario alignment or antialignment emerges purely from the dynamics of elastically interacting objects with off-centered masses.

## APPENDIX B: SELF-ALIGNING ACTIVE PARTICLE IN A HARMONIC POTENTIAL WITH ISOTROPIC DAMPING

### 1. General model

After rescaling the equations of motion are given by:

$$\dot{\mathbf{r}} = \hat{\mathbf{n}} - \mathbf{r}, \quad (\text{B1a})$$

$$\dot{\theta} = \beta |\mathbf{v}|^\nu f[(\hat{\mathbf{n}} \times \hat{\mathbf{v}}) \cdot \hat{\mathbf{z}}], \quad (\text{B1b})$$

where  $f[x]$  is a nonsingular odd function with a domain given by  $x \in [-1, 1]$ . The cases considered in the literature include  $f[x] = x$  and  $f[x] = \sin^{-1}(x)$ . The exponent  $\nu$  is non-negative; in the literature the values used are  $\nu = 0$  and  $1$ .

Using the rotational invariance, one describes a given state using the distance  $r$  to the origin and the angle  $\phi$  between the position and the orientation. If  $\alpha$  is the angle of the position,  $\phi$  is given by  $\phi = \theta - \alpha$ . Projecting Eq. (B1a) on  $\mathbf{r}$  and  $\mathbf{r}^\perp$ , we get  $\dot{r} = \cos(\phi) - r$  and  $r\dot{\alpha} = \sin(\phi)$ . Using these two projections, we can get the norm of the velocity,  $|\mathbf{v}| = \sqrt{1 + r^2 - 2r \cos(\phi)}$ , and the vector product,

$$\begin{aligned} (\hat{\mathbf{n}} \times \hat{\mathbf{v}}) \cdot \hat{\mathbf{z}} &= -(\hat{\mathbf{n}} \times \mathbf{r}) \cdot \hat{\mathbf{z}} / |\mathbf{v}| \\ &= r \sin(\phi) / \sqrt{1 + r^2 - 2r \cos(\phi)}. \end{aligned}$$

Finally, we get

$$\dot{r} = \cos(\phi) - r, \quad (\text{B2a})$$

$$\begin{aligned} \dot{\phi} &= \beta [1 + r^2 - 2r \cos(\phi)]^{\nu/2} f \left[ \frac{r \sin(\phi)}{\sqrt{1 + r^2 - 2r \cos(\phi)}} \right] \\ &\quad - \frac{\sin(\phi)}{r}. \end{aligned} \quad (\text{B2b})$$

### 2. Stationary solutions

We now consider stationary solutions that satisfy  $\dot{r} = 0$  and  $\dot{\phi} = 0$ . These contain the frozen state where  $r = 1$  and  $\phi = 0$  and chiral states where  $\phi \neq 0$ . From  $\dot{r} = 0$  we get  $r = \cos(\phi)$ , and inserting this relation into  $\dot{\phi} = 0$ , we get

$$\beta |\sin(\phi)|^{\nu/2} f \left[ \frac{r \sin(\phi)}{|\sin(\phi)|} \right] = \tan(\phi). \quad (\text{B3})$$

Since  $f(x)$  is odd,  $-\phi$  is a solution if  $\phi$  is a solution; we thus assume that  $\phi \geq 0$  and use  $\cos(\phi) = r$  and  $\sin(\phi) = \sqrt{1 - r^2}$  to get an equation for  $r$ ,

$$\beta(1-r^2)^{\nu/2}f[r] = \frac{\sqrt{1-r^2}}{r}. \quad (\text{B4})$$

The frozen state corresponding to  $r = 1$  and  $\phi = 0$  is a solution for  $\nu > 0$ . Chiral states corresponding to  $r < 1$  satisfy

$$\beta f[r] = \frac{(1-r^2)^{(1-\nu)/2}}{r}. \quad (\text{B5})$$

For  $\nu < 1$  there is always a solution: chiral states exist for all values of  $\beta$ . For  $\nu = 1$ , chiral states exist if  $\beta > 1/f[1]$ . For  $\nu > 1$ , zero, one, or two chiral states may exist, depending on the value of  $\beta$ .

### 3. Stability analysis of the frozen state

We perform a stability analysis on the frozen state for  $\nu > 0$ . We assume that  $r_1 = r - 1 \ll 1$  and  $\phi \ll 1$  and use these expansions in Eqs. (B2a) and (B2b). At the lowest order,

$$\dot{r}_1 = -r_1 - \frac{\phi^2}{2}, \quad (\text{B6})$$

$$\dot{\phi} = \beta(r_1^2 + \phi^2)^{\nu/2}f\left[\frac{\phi}{\sqrt{r_1^2 + \phi^2}}\right] - \phi. \quad (\text{B7})$$

Considering positive values for  $\phi$ , we see that if  $f(x) \geq ax$  (which is the case for the two situations considered here),

$$\dot{\phi} \geq [\beta a(r_1^2 + \phi^2)^{(\nu-1)/2} - 1]\phi. \quad (\text{B8})$$

For  $\nu < 1$ , the first term in brackets is large, meaning that the orientation dynamics is unstable.

### 4. Conclusion

We conclude that for  $\nu < 1$  chiral states are observed for all the values of the alignment parameter  $\beta$ , while for  $\nu = 1$  they are observed only beyond a certain value. The situation is more complicated for  $\nu > 0$ , as multiple chiral states exist, with some of them stable and others unstable.

## APPENDIX C: SELF-ALIGNING ACTIVE PARTICLE IN A HARMONIC POTENTIAL WITH ANISOTROPIC DAMPING

### 1. General model

The equation of motion for the position vector  $\mathbf{r}$  in the presence of anisotropic damping after rescaling is given by

$$\dot{\mathbf{r}} = \hat{\mathbf{n}} - \mathbb{M}\mathbf{r}. \quad (\text{C1})$$

In this context  $\mathbb{M}$  represents the mobility matrix, which is defined as  $\mathbb{M} = \mu_{\parallel}\hat{\mathbf{n}}\hat{\mathbf{n}} + \mu_{\perp}(\mathbb{I} - \hat{\mathbf{n}}\hat{\mathbf{n}})$ . We express the mobility matrix in terms of a single control parameter  $\chi$ , which is defined as  $\mu_{\parallel} = (1+\chi)$  and  $\mu_{\perp} = (1-\chi)$ . For  $\chi = 0$ , the equation of motion simplifies to the isotropic damping case, which is expressed as  $\dot{\mathbf{r}} = \hat{\mathbf{n}} - \mathbf{r}$ . Conversely, for  $\chi = 1$  it simplifies to  $\dot{\mathbf{r}} = [1 - 2(\mathbf{r} \cdot \hat{\mathbf{n}})]\hat{\mathbf{n}}$ . Projecting onto  $\mathbf{r}$  and  $\mathbf{r}^{\perp}$ , we

obtain

$$\begin{aligned} \dot{r} &= [1 - (1+\chi)r\cos(\phi)]\cos(\phi) \\ &\quad - (1-\chi)r\sin(\phi)\sin(\phi), \\ \dot{r}\dot{\alpha} &= [1 - (1+\chi)r\cos(\phi)]\sin(\phi) \\ &\quad + (1-\chi)r\sin(\phi)\cos(\phi). \end{aligned} \quad (\text{C2})$$

The orientation angle, which evolves with self-alignment, is given by  $\dot{\theta} = \beta(\hat{\mathbf{n}} \times \mathbf{f}) \cdot \hat{\mathbf{z}}$ , which simplifies to

$$\dot{\theta} = -\beta(\hat{\mathbf{n}} \times \mathbf{r}) \cdot \hat{\mathbf{z}}. \quad (\text{C3})$$

Finally, we can write the  $\phi = \theta - \alpha$  dynamical equation as

$$\begin{aligned} \dot{\phi} &= \left[ \frac{\beta r^2 - 1}{r} + (1+\chi)\cos(\phi) \right] \sin(\phi) \\ &\quad - (1-\chi)\sin(\phi)\cos(\phi). \end{aligned} \quad (\text{C4})$$

### 2. Stationary solutions

We obtain the stationary solutions for Eqs. (C2)–(C4) by setting  $\dot{r} = 0$  and  $\dot{\phi} = 0$ . These solutions include the frozen state, characterized here by  $\phi = 0$  and  $r = 1/(1+\chi)$ , as well as chiral states with  $\phi \neq 0$ .

Imposing  $\dot{r} = 0$ , we find that  $r = \cos(\phi)/[1 + \chi \cos(2\phi)]$ . Inserting this relation into  $\dot{\phi} = 0$ , we obtain

$$\begin{aligned} \beta\cos^2(\phi) &= [1 + \chi \cos(2\phi)]\{[1 + \chi \cos(2\phi)] \\ &\quad - 2\chi \sin(\phi)\cos^2(\phi)\}. \end{aligned} \quad (\text{C5})$$

For isotropic damping with  $\chi = 0$ , the corresponding solutions are  $\beta\cos^2(\phi) = 1$  and  $\beta r^2 = 1$ . For the fully anisotropic damping case with  $\chi = 1$ , the solutions are  $\beta = 4\cos^2(\phi)[1 - \sin(\phi)]$  and  $\beta r^2 = (1 - \sqrt{1 - (1/2r)^2})$ .

### 3. Conclusion

Anisotropic damping can strongly change the dynamics of self-aligning active agents. A complete theoretical exploration of its impact, even in the simplest case of a single self-aligning particle in a harmonic potential, has yet to be developed.

## REFERENCES

- Abercrombie, M., and J. E. Heaysman, 1954, *Exp. Cell Res.* **6**, 293.
- Alaimo, F., S. Praetorius, and A. Voigt, 2016, *New J. Phys.* **18**, 083008.
- Alert, R., J. Casademunt, and J.-F. Joanny, 2022, *Annu. Rev. Condens. Matter Phys.* **13**, 143.
- Alert, R., and X. Trepaut, 2020, *Annu. Rev. Condens. Matter Phys.* **11**, 77.
- Anderson, J. L., 1989, *Annu. Rev. Fluid Mech.* **21**, 61.
- Angelini, T. E., E. Hannezo, X. Trepaut, M. Marquez, J. J. Fredberg, and D. A. Weitz, 2011, *Proc. Natl. Acad. Sci. U.S.A.* **108**, 4714.
- Baconnier, P., 2023, Ph.D. thesis (Université Paris Sciences et Lettres).

- Baconnier, P., V. Démery, and O. Dauchot, 2024, *Phys. Rev. E* **109**, 024606.
- Baconnier, P., D. Shohat, C. H. López, C. Coulais, V. Démery, G. Düring, and O. Dauchot, 2022, *Nat. Phys.* **18**, 1234.
- Bahl, S., H. Nagar, I. Singh, and S. Sehgal, 2020, *Mater. Today Proc.* **28**, 1302.
- Barré, J., R. Chétrite, M. Muratori, and F. Peruani, 2015, *J. Stat. Phys.* **158**, 589.
- Barton, D. L., S. Henkes, C. J. Weijer, and R. Sknepnek, 2017, *PLoS Comput. Biol.* **13**, e1005569.
- Benveniste, B., O. Granek, S. Ro, R. Yaacoby, H. Chaté, Y. Kafri, D. Mukamel, A. Solon, and J. Tailleur, 2023, *Phys. Rev. Lett.* **131**, 218301.
- Ben Zion, M. Y., J. Fersula, N. Bredeche, and O. Dauchot, 2023, *Sci. Rob.* **8**, eab6140.
- Bertin, E., H. Chaté, F. Ginelli, S. Mishra, A. Peshkov, and S. Ramaswamy, 2013, *New J. Phys.* **15**, 085032.
- Bertin, E., M. Droz, and G. Grégoire, 2009, *J. Phys. A* **42**, 445001.
- Besse, M., H. Chaté, and A. Solon, 2022, *Phys. Rev. Lett.* **129**, 268003.
- Bi, D., X. Yang, M. C. Marchetti, and M. L. Manning, 2016, *Phys. Rev. X* **6**, 021011.
- Bialké, J., H. Löwen, and T. Speck, 2013, *Europhys. Lett.* **103**, 30008.
- Boltzmann, L., 1872, *Weitere Studien über das Wärmegleichgewicht unter Gasmolekülen*, Vol. 66 (Aus der k. k. Hot- und Staatsdruckerei, Vienna), pp. 275–370.
- Brambilla, M., E. Ferrante, M. Birattari, and M. Dorigo, 2013, *Swarm Intell.* **7**, 1.
- Briand, G., and O. Dauchot, 2016, *Phys. Rev. Lett.* **117**, 098004.
- Briand, G., M. Schindler, and O. Dauchot, 2018, *Phys. Rev. Lett.* **120**, 208001.
- Bricard, A., J.-B. Caussin, N. Desreumaux, O. Dauchot, and D. Bartolo, 2013, *Nature (London)* **503**, 95.
- Brückner, D. B., M. Schmitt, A. Fink, G. Ladurner, J. Flommersfeld, N. Arlt, E. Hannezo, J. O. Rädler, and C. P. Broedersz, 2022, *Phys. Rev. X* **12**, 031041.
- Bull, M. S., V. N. Prakash, and M. Prakash, 2021, arXiv:2107.02934.
- Camley, B. A., and W.-J. Rappel, 2014, *Phys. Rev. E* **89**, 062705.
- Canavello, D., R. H. Damascena, L. R. E. Cabral, and C. C. de Souza Silva, 2024, *Soft Matter* **20**, 2310.
- Casiulis, M., E. Arbel, Y. Lahini, S. Martiniani, N. Oppenheimer, and M. Y. B. Zion, 2024, arXiv:2409.04618.
- Casiulis, M., M. Tarzia, L. F. Cugliandolo, and O. Dauchot, 2020, *Phys. Rev. Lett.* **124**, 198001.
- Cates, M. E., and J. Tailleur, 2015, *Annu. Rev. Condens. Matter Phys.* **6**, 219.
- Cavagna, A., and I. Giardina, 2014, *Annu. Rev. Condens. Matter Phys.* **5**, 183.
- Chiang, M., A. Hopkins, B. Loewe, M. C. Marchetti, and D. Marenduzzo, 2024, *Proc. Natl. Acad. Sci. U.S.A.* **121**, e2319310121.
- Dalhaimer, P., D. E. Discher, and T. C. Lubensky, 2007, *Nat. Phys.* **3**, 354.
- Damascena, R. H., L. R. E. Cabral, and C. C. de Souza Silva, 2022, *Phys. Rev. E* **105**, 064608.
- Das, S., M. Ciarchi, Z. Zhou, J. Yan, J. Zhang, and R. Alert, 2024, *Phys. Rev. X* **14**, 031008.
- Dauchot, O., and V. Démery, 2019, *Phys. Rev. Lett.* **122**, 068002.
- Davidescu, M. R., P. Romanczuk, T. Gregor, and I. D. Couzin, 2023, *Proc. Natl. Acad. Sci. U.S.A.* **120**, e2206163120.
- Dean, D. S., 1996, *J. Phys. A* **29**, L613.
- Deforet, M., V. Hakim, H. G. Yevick, G. Duclos, and P. Silberzan, 2014, *Nat. Commun.* **5**, 3747.
- Deseigne, J., O. Dauchot, and H. Chaté, 2010, *Phys. Rev. Lett.* **105**, 098001.
- Deseigne, J., S. Léonard, O. Dauchot, and H. Chaté, 2012, *Soft Matter* **8**, 5629.
- Doostmohammadi, A., J. Ignés-Mullol, J. M. Yeomans, and F. Sagués, 2018, *Nat. Commun.* **9**, 3246.
- Doostmohammadi, A., S. P. Thampi, and J. M. Yeomans, 2016, *Phys. Rev. Lett.* **117**, 048102.
- Doxzen, K., S. R. K. Vedula, M. C. Leong, H. Hirata, N. S. Gov, A. J. Kabla, B. Ladoux, and C. T. Lim, 2013, *Integr. Biol.* **5**, 1026.
- Farhadifar, R., J.-C. Röper, B. Aigouy, S. Eaton, and F. Jülicher, 2007, *Curr. Biol.* **17**, 2095.
- Ferrante, E., A. E. Turgut, M. Dorigo, and C. Huepe, 2013a, *New J. Phys.* **15**, 095011.
- Ferrante, E., A. E. Turgut, M. Dorigo, and C. Huepe, 2013b, *Phys. Rev. Lett.* **111**, 268302.
- Ferrante, E., A. E. Turgut, C. Huepe, A. Stranieri, C. Pincioli, and M. Dorigo, 2012, *Adapt. Behav.* **20**, 460.
- Fersula, J., N. Bredeche, and O. Dauchot, 2024, *Phys. Rev. E* **110**, 014606.
- Fletcher, A. G., M. Osterfield, R. E. Baker, and S. Y. Shvartsman, 2014, *Biophys. J.* **106**, 2291.
- Fruchart, M., R. Hanai, P. B. Littlewood, and V. Vitelli, 2021, *Nature (London)* **592**, 363.
- Garattoni, L., and M. Birattari, 2016, in *Wiley Encyclopedia of Electrical and Electronics Engineering*, Vol. 10, edited by J. G. Webster (John Wiley & Sons, New York).
- Giazzazi, F., C. Malinverno, S. Corallino, F. Ginelli, G. Scita, and R. Cerbino, 2017, *J. Phys. D* **50**, 384003.
- Giazzazi, F., M. Paoluzzi, M. Macchi, D. Bi, G. Scita, M. L. Manning, R. Cerbino, and M. C. Marchetti, 2018, *Soft Matter* **14**, 3471.
- Ginelli, F., F. Peruani, M. Bär, and H. Chaté, 2010, *Phys. Rev. Lett.* **104**, 184502.
- Ginelli, F., F. Peruani, M.-H. Pillot, H. Chaté, G. Theraulaz, and R. Bon, 2015, *Proc. Natl. Acad. Sci. U.S.A.* **112**, 12729.
- Giomi, L., N. Hawley-Weld, and L. Mahadevan, 2013, *Proc. R. Soc. A* **469**, 20120637.
- Granek, O., Y. Kafri, M. Kardar, S. Ro, J. Tailleur, and A. Solon, 2024, *Rev. Mod. Phys.* **96**, 031003.
- Grossman, D., I. Aranson, and E. B. Jacob, 2008, *New J. Phys.* **10**, 023036.
- Henkes, S., Y. Fily, and M. C. Marchetti, 2011, *Phys. Rev. E* **84**, 040301.
- Henkes, S., K. Kostanjevec, J. M. Collinson, R. Sknepnek, and E. Bertin, 2020, *Nat. Commun.* **11**, 1405.
- Henkes, S., M. C. Marchetti, and R. Sknepnek, 2018, *Phys. Rev. E* **97**, 042605.
- Hernández-López, C., P. Baconnier, C. Coulais, O. Dauchot, and G. Düring, 2024, *Phys. Rev. Lett.* **132**, 238303.
- Huepe, C., E. Ferrante, T. Wenseleers, and A. E. Turgut, 2015, *J. Stat. Phys.* **158**, 549.
- Janssen, L. M., 2019, *J. Phys. Condens. Matter* **31**, 503002.
- Jülicher, F., S. W. Grill, and G. Salbreux, 2018, *Rep. Prog. Phys.* **81**, 076601.
- Jülicher, F., K. Kruse, J. Prost, and J.-F. Joanny, 2007, *Phys. Rep.* **449**, 3.
- Killeen, A., T. Bertrand, and C. F. Lee, 2022, *Phys. Rev. Lett.* **128**, 078001.
- Kness, M., L. S. Tuckerman, and D. Barkley, 1992, *Phys. Rev. A* **46**, 5054.

- Kruse, K., J. F. Joanny, F. Jülicher, J. Prost, and K. Sekimoto, 2004, *Phys. Rev. Lett.* **92**, 078101.
- Kruse, K., J.-F. Joanny, F. Jülicher, J. Prost, and K. Sekimoto, 2005, *Eur. Phys. J. E* **16**, 5.
- Ladoux, B., and R.-M. Mège, 2017, *Nat. Rev. Mol. Cell Biol.* **18**, 743.
- Lam, K.-D. N. T., M. Schindler, and O. Dauchot, 2015a, *J. Stat. Mech.* P10017.
- Lam, K.-D. N. T., M. Schindler, and O. Dauchot, 2015b, *New J. Phys.* **17**, 113056.
- Lazzari, D., O. Dauchot, and C. Brito, 2024, arXiv:2407.13682.
- Lin, G., Z. Han, and C. Huepe, 2021, *New J. Phys.* **23**, 023019.
- Lin, G., Z. Han, A. Shee, and C. Huepe, 2023, *Phys. Rev. Lett.* **131**, 168301.
- Liu, S., S. Shankar, M. C. Marchetti, and Y. Wu, 2021, *Nature (London)* **590**, 80.
- Löwen, H., 2020, *J. Chem. Phys.* **152**, 040901.
- Maitra, A., and S. Ramaswamy, 2019, *Phys. Rev. Lett.* **123**, 238001.
- Malinverno, C., *et al.*, 2017, *Nat. Mater.* **16**, 587.
- Marchetti, M. C., J. F. Joanny, S. Ramaswamy, T. B. Liverpool, J. Prost, M. Rao, and R. A. Simha, 2013, *Rev. Mod. Phys.* **85**, 1143.
- Menzel, A. M., and H. Löwen, 2013, *Phys. Rev. Lett.* **110**, 055702.
- Menzel, A. M., and T. Ohta, 2012, *Europhys. Lett.* **99**, 58001.
- Mermin, N. D., 1968, *Phys. Rev.* **176**, 250.
- Monfared, S., G. Ravichandran, J. Andrade, and A. Doostmohammadi, 2023, *eLife* **12**, e82435.
- Morin, A., N. Desreumaux, J.-B. Caussin, and D. Bartolo, 2017, *Nat. Phys.* **13**, 63.
- Nagai, T., and H. Honda, 2001, *Philos. Mag. B* **81**, 699.
- Narinder, N., C. Bechinger, and J. R. Gomez-Solano, 2018, *Phys. Rev. Lett.* **121**, 078003.
- Newman, M., 2010, *Networks: An Introduction* (Oxford University Press, Oxford).
- Niwa, H.-S., 1994, *J. Theor. Biol.* **171**, 123.
- Notbohm, J., S. Banerjee, K. J. Utuje, B. Gweon, H. Jang, Y. Park, J. Shin, J. P. Butler, J. J. Fredberg, and M. C. Marchetti, 2016, *Biophys. J.* **110**, 2729.
- Ophaus, L., S. V. Gurevich, and U. Thiele, 2018, *Phys. Rev. E* **98**, 022608.
- Paoluzzi, M., D. Levis, and I. Pagonabarraga, 2024, *Commun. Phys.* **7**, 57.
- Park, J.-A., *et al.*, 2015, *Nat. Mater.* **14**, 1040.
- Peruani, F., A. Deutsch, and M. Bär, 2006, *Phys. Rev. E* **74**, 030904.
- Peruani, F., T. Klauss, A. Deutsch, and A. Voss-Boehme, 2011, *Phys. Rev. Lett.* **106**, 128101.
- Peshkov, A., E. Bertin, F. Ginelli, and H. Chaté, 2014, *Eur. Phys. J. Special Topics* **223**, 1315.
- Petrolli, V., *et al.*, 2019, *Phys. Rev. Lett.* **122**, 168101.
- Peyret, G., R. Mueller, J. d'Alessandro, S. Begnaud, P. Marcq, R.-M. Mège, J. M. Yeomans, A. Doostmohammadi, and B. Ladoux, 2019, *Biophys. J.* **117**, 464.
- Pfeifer, R., 2006, *How the Body Shapes the Way We Think: A New View of Intelligence* (MIT Press, Cambridge, MA).
- Premlata, A. R., and H.-H. Wei, 2021, *Phys. Fluids* **33**, 112003.
- Ramaswamy, S., 2010, *Annu. Rev. Condens. Matter Phys.* **1**, 323.
- Ramaswamy, S., R. A. Simha, and J. Toner, 2003, *Europhys. Lett.* **62**, 196.
- Romanczuk, P., I. D. Couzin, and L. Schimansky-Geier, 2009, *Phys. Rev. Lett.* **102**, 010602.
- Rozman, J., J. M. Yeomans, and R. Sknepnek, 2023, *Phys. Rev. Lett.* **131**, 228301.
- Rubenstein, M., A. Cornejo, and R. Nagpal, 2014, *Science* **345**, 795.
- Saw, T. B., A. Doostmohammadi, V. Nier, L. Kocgozlu, S. Thampi, Y. Toyama, P. Marcq, C. T. Lim, J. M. Yeomans, and B. Ladoux, 2017, *Nature (London)* **544**, 212.
- Schaller, V., C. Weber, C. Semmrich, E. Frey, and A. R. Bausch, 2010, *Nature (London)* **467**, 73.
- Scheibner, C., A. Souslov, D. Banerjee, P. Surówka, W. T. Irvine, and V. Vitelli, 2020, *Nat. Phys.* **16**, 475.
- Scholz, C., S. Jahanshahi, A. Ldov, and H. Löwen, 2018, *Nat. Commun.* **9**, 5156.
- Sese-Sansa, E., I. Pagonabarraga, and D. Levis, 2018, *Europhys. Lett.* **124**, 30004.
- Shimoyama, N., K. Sugawara, T. Mizuguchi, Y. Hayakawa, and M. Sano, 1996, *Phys. Rev. Lett.* **76**, 3870.
- Sknepnek, R., I. Djafer-Cherif, M. Chuai, C. Weijer, and S. Henkes, 2023, *eLife* **12**, e79862.
- Smeets, B., R. Alert, J. Pešek, I. Pagonabarraga, H. Ramon, and R. Vincent, 2016, *Proc. Natl. Acad. Sci. U.S.A.* **113**, 14621.
- Solon, A., H. Chaté, J. Toner, and J. Tailleur, 2022, *Phys. Rev. Lett.* **128**, 208004.
- Spillman, Jr., W. B., J. S. Sirkis, and P. T. Gardiner, 1996, *Smart Mater. Struct.* **5**, 247.
- Sprenger, A. R., L. Caprini, H. Löwen, and R. Wittmann, 2023, *J. Phys. Condens. Matter* **35**, 305101.
- Stramer, B., and R. Mayor, 2017, *Nat. Rev. Mol. Cell Biol.* **18**, 43.
- Swan, J. W., and A. S. Khair, 2008, *J. Fluid Mech.* **606**, 115.
- Szabó, B., G. J. Szöllösi, B. Gönci, Z. Jurányi, D. Selmeczi, and T. Vicsek, 2006, *Phys. Rev. E* **74**, 061908.
- Tambe, D. T., *et al.*, 2011, *Nat. Mater.* **10**, 469.
- Tang, W., Y. Zheng, A. Shee, G. Lin, Z. Han, P. Romanczuk, and C. Huepe, 2024, arXiv:2410.13705.
- Teixeira, E. F., H. C. Fernandes, and L. G. Brunnet, 2021, *Soft Matter* **17**, 5991.
- te Vrugt, M., H. Löwen, and R. Wittkowski, 2020, *Adv. Phys.* **69**, 121.
- Tjhung, E., C. Nardini, and M. E. Cates, 2018, *Phys. Rev. X* **8**, 031080.
- Toner, J., and Y. Tu, 1995, *Phys. Rev. Lett.* **75**, 4326.
- Toner, J., Y. Tu, and S. Ramaswamy, 2005, *Ann. Phys. (Amsterdam)* **318**, 170.
- Turgut, A. E., I. C. Boz, I. E. Okay, E. Ferrante, and C. Huepe, 2020, *J. R. Soc. Interface* **17**, 20200165.
- Vicsek, T., A. Czirók, E. Ben-Jacob, I. Cohen, and O. Shochet, 1995, *Phys. Rev. Lett.* **75**, 1226.
- Vicsek, T., and A. Zafeiris, 2012, *Phys. Rep.* **517**, 71.
- Weber, C. A., T. Hanke, J. Deseigne, S. Léonard, O. Dauchot, E. Frey, and H. Chaté, 2013, *Phys. Rev. Lett.* **110**, 208001.
- Wittkowski, R., A. Tiribocchi, J. Stenhammar, R. J. Allen, D. Marenduzzo, and M. E. Cates, 2014, *Nat. Commun.* **5**, 4351.
- Woodhouse, F. G., H. Ronellenfitsch, and J. Dunkel, 2018, *Phys. Rev. Lett.* **121**, 178001.
- Xu, H., Y. Huang, R. Zhang, and Y. Wu, 2023, *Nat. Phys.* **19**, 46.
- Yllanes, D., M. Leoni, and M. Marchetti, 2017, *New J. Phys.* **19**, 103026.
- Zhang, H.-P., A. Be'er, E.-L. Florin, and H. L. Swinney, 2010, *Proc. Natl. Acad. Sci. U.S.A.* **107**, 13626.
- Zhang, J., R. Alert, J. Yan, N. S. Wingreen, and S. Granick, 2021, *Nat. Phys.* **17**, 961.
- Zheng, E., M. Brandenbourger, L. Robinet, P. Schall, E. Lerner, and C. Coulais, 2023, *Phys. Rev. Lett.* **130**, 178202.
- Zheng, Y., C. Huepe, and Z. Han, 2020, *Adapt. Behav.* **30**, 19.